Master's Thesis

Department of Physics
Institute for Marine and Atmospheric research Utrecht

Universiteit Utrecht

A Conceptual Model Perspective on the Coupling of El Niño–Southern Oscillation and Global Mean Surface Temperature

First examiner
Prof. dr. ir. Henk A. Dijkstra

Second examiner
Dr. Claudia E. Wieners

Candidate
Bennet Niklas Weiss

Program
Climate Physics

June 30, 2024

Abstract

El Niño-Southern Oscillation (ENSO), the most energetic source of inter-annual climate variability, affects not only the regional climate in its tropical Pacific origin but also the global climate. During El Niño events, elevated sea surface temperatures (SSTs) in the eastern equatorial Pacific release excess heat into the atmosphere, leading to a delayed warming of the global mean surface temperature (GMST). In the context of a warming climate with increasing GMST, ENSO is expected to change, but the exact nature of this change remains uncertain. To capture the bidirectional relationship of ENSO and GMST, we developed a simple full-field model for GMST and coupled it to an existing conceptual model for ENSO through SSTs and radiative-convective equilibrium (RCE) temperature. Our model shows a reduced frequency of El Niño events but stronger individual occurrences in a warmer climate. The response of GMST to ENSO remains approximately constant at around 0.12 °C per degree of Niño 3.4 index with a lag of about four months. Contrary to projections from most general circulation models (GCM) that simulate a weakened zonal SST gradient and trade winds in a warming climate, our results indicate an increasing zonal SST gradient and stronger westerlies sustained by cool eastern Pacific subsurface temperatures; findings that are generally supported by reanalysis data from recent decades. By leveraging the conceptual nature of our ENSO-GMST model, we explore the physical mechanisms behind this behavior, offering an intra-tropical Pacific view on these mean state changes.

Acknowledgement

This thesis marks the end of my master's at Utrecht University and, with that, also represents the conclusion of my student life. My time at IMAU, and during this project in particular, has been made unique by the people I have met and worked with. I would like to thank my supervisor, Henk Dijkstra, for his guidance and support throughout this venture. I also want to extend my thanks to Claudia Wieners for providing me with expert feedback during the project's final stage. A special thanks goes to Romain Veltz for his generous support regarding the proper use of his bifurcation analysis tool. I am very grateful for the opportunity to have been part of the institute's ocean group and to have studied and worked alongside fun and talented fellow students. I want to explicitly thank my friends that had the patience to read and discuss my work, especially during the final stages of this project. I also appreciate the many discussions about physics - both related and unrelated to my thesis - I have had with Stan, which also helped propel my project further. Lastly, I am deeply appreciative of the special friendships I have made here with Jeroen, Lasse, Lupi, Chiara and Cormac and I am especially grateful to Jassi and my family for their continuous support, encouragement, and love.

1 Introduction

El Niño-Southern Oscillation (ENSO) is the most energetic source of inter-annual climate variability (Singh, 2012), and only the seasonal cycle is more important for short-term climate variability (Goddard & Dilley, 2005). ENSO refers to a quasiperiodic oscillation of the climate, occurring with a period of approximately 2-8 years (Torrence & Compo, 1998). Its origins lie in the equatorial Pacific, whose mean state is characterized by a strong zonal gradient in sea surface temperature (SST), with a "warm pool" in the west and a "cold tongue" in the east. During El Niño, SSTs in the cold tongue are higher than average, while La Niña describes a state of lower than usual SSTs in that region (Dijkstra, 2013). By averaging SST anomalies in the Niño 3.4 region defined by 5°S-5°N and 170°W-120°W, this variability can be monitored, quantifying the oceanic component of ENSO. In the equatorial Pacific, atmospheric pressure and surface winds are closely connected to the SST (Dijkstra, 2013), creating atmospheric interannual variability - the Southern Oscillation. These winds have a strong influence on the ocean, creating a feedback loop first described by Bjerknes (1969). Consequently, the atmospheric Southern Oscillation and oceanic El Niño are closely linked, together forming the coupled ocean-atmosphere phenomenon known as ENSO.

Impacts of ENSO are significant and far-reaching: rain-patterns over the equatorial Pacific shift eastward during El Niño, promoting droughts and forest fires at the western boundary of the equatorial Pacific but rainfall and floods in the east (W. Cai et al., 2021). Due to its influence extending into the stratosphere, ENSO is associated with world-wide climatic changes such as higher surface temperatures over western Canada and Alaska, cooling in parts of the Middle East, North Africa and northern India, or increased precipitation over the United States of America through long-distance teleconnections (Alizadeh, 2024). On the one hand, ENSO extremes therefore drive devastating events with significant consequences, while on the other hand increasing seasonal predictability (Tang et al., 2018) offering potential for targeted vulnerability reduction (Goddard & Dilley, 2005).

Global mean surface temperature (GMST) increases in the order of $\sim 0.1\,^{\circ}\mathrm{C}$ in response to an El Niño event (Trenberth et al., 2002). This feedback depends on the strength of the event, reaching beyond $0.2\,^{\circ}\mathrm{C}$ after an exceptionally strong El Niño, as was the case during the event in 1997 – 1998 (Foster & Rahmstorf, 2011). In consequence, record-breaking surface temperatures are more likely to occur in a year with a strong El Niño (Su et al., 2017) - a trend that is expected to strengthen in a high-emission scenario (Hsu & Yin, 2019). From simple scale analysis it is clear that the GMST response to ENSO is one order of magnitude stronger than could be expected from the area of SST variability associated with ENSO (Hu & Fedorov, 2017). Consequently, it is indispensable to consider atmospheric heating mechanisms in order to understand and model atmospheric temperature responses to ENSO. Previous studies have exploited idealized models to connect observed SST anomalies to mean temperature anomalies in the tropics (Yulaeva & Wallace, 1994) and globally (Hu & Fedorov, 2017; Thompson et al., 2009), or used statistical techniques like regression to factor out the ENSO signal from regional (Chen et al., 2008) and global temperatures (Trenberth et al., 2002; Wigley, 2000), or employed other statistical techniques as listed in Thompson et al. (2009).

The relationship of ENSO and GMST is however not unidirectional. In a changing climate characterized by rising GMST, ENSO is expected to change (W. Cai et al., 2021). Emerging model consensus combined with paleoclimatic evidence points towards increased ENSO-related SST variability in the future, lifting the probability for intense El Niño and La Niña events (W. Cai et al., 2021). However, model biases and contradicting observational evidence complicate the picture and reduce confidence in these projections (W. Cai et al., 2021). For example, most general circulation models (GCMs) project a decreased equatorial Pacific SST gradient accompanied by a weakening of the Pacific Walker circulation (W. Cai et al., 2021), an atmospheric overturning cell with the easterly trade winds as its surface manifestation. However, reanalysis data reveals opposite trends in recent decades (Alizadeh, 2024; W. Cai et al., 2021). Paleoproxy data suggests that the recent amplification of the Pacific Walker circulation is not unprecedented in the context of the last millennium (Falster et al., 2023), and previous

studies indicate that internal variability (Zhao & Allen, 2019) and inter-basin interaction - for example with the Atlantic (McGregor et al., 2014) - may be the main drivers of this strengthening, potentially making this trend transient (W. Cai et al., 2021). The analysis of these underlying mechanisms is however complicated by discrepancies between reanalysis and satellite data (Chung et al., 2019), as well as by the dependence on the selected time period (Kosovelj & Zaplotnik, 2023). Furthermore, a changing background climate might not only influence ENSO itself, but also alter the impact of ENSO on the global climate system (Alizadeh, 2024).

In this work, we revisit the dynamic interplay of ENSO and GMST. By using a full-field conceptual coupled ENSO-GMST model, we capture the holistic bidirectional connection between the two, which was unavailable in previous studies of the GMST response to ENSO from Hu and Fedorov (2017) or Thompson et al. (2009). This allows us to investigate how ENSO responds to a changing climate characterized by GMST. Additionally, we explore the impact of tropical Pacific SST variability on GMST, and analyze the state dependency of this feedback. Conceptual models like the one used in this work are more easily interpretable than complex GCMs (Dijkstra, 2024; Dijkstra & Burgers, 2002), while also being vastly cheaper to operate. By leveraging the simple model structure, we can unravel some of the underlying mechanisms behind the changes of ENSO and therefore offer an intra-tropical Pacific view on the influence of climate change.

This thesis is structured as follows: in Section 2 we present the data used and preprocessing steps applied. Section 3 introduces the ENSO-GMST model by describing each component and the coupling in detail. Section 4 describes the methodology to generate the model results presented in Section 5, which includes an analysis of model mean state, ENSO characteristics, and GMST response for changing radiative forcing through CO_2. Lastly, Section 6 summarizes the findings and discusses their implications.

2 Data

This section gives an overview of data sources and preprocessing steps before they were applied to train our model or used in further analysis. All data used in this study has a time resolution of one month and covers the period from 1980-2023, representing the largest common time period of the datasets. This period does not only benefit from the available satellite data improving reanalysis products (Foster & Rahmstorf, 2011) but also represents the current ENSO conditions well, as it starts just after the cold-to-warm shift of equatorial SST in 1976/77 associated with the Pacific Decadal Oscillation (PDO) (Jacques-Coper & Garreaud, 2015). An overview of the time series of the data used is given in Figure 1. In the following paragraphs, we present all data sources and processing steps in more detail.

For carbon dioxide concentrations, monthly trends of globally averaged marine surface concentrations from the National Oceanic and Atmospheric Administration (NOAA) (Lan et al., 2023) were used. The global mean of aerosol optical depth (AOD) is a latitude-weighted average of data from MERRA-2 (Global Modeling And Assimilation Office (GMAO), 2015). AOD was transformed into anomalies by subtracting the average value for each month individually, i.e., removing the period's climatology.

Further data originates from the ERA5 global reanalysis product (Hersbach et al., 2023), which contains monthly averages of important climate variables on a 0.25° grid. For GMST, the 2 meter air temperature was averaged globally. SST was readily available from ERA5. It is used for shading in Figure 2, where the standard deviation was calculated point-wise without any other processing. Additionally, in order to obtain regional means, SST was averaged in the Niño 3.4 region as well as within the specified region in the western (WP), central (CP) and eastern (EP) equatorial Pacific, respectively (Fang et al., 2024). The WP, CP and EP regions are meridionally confined by ±5°N and span the Pacific Ocean from 120 °E - 170 °E, 170 °E - 140 °W and 140 °W - 80 °W, respectively.

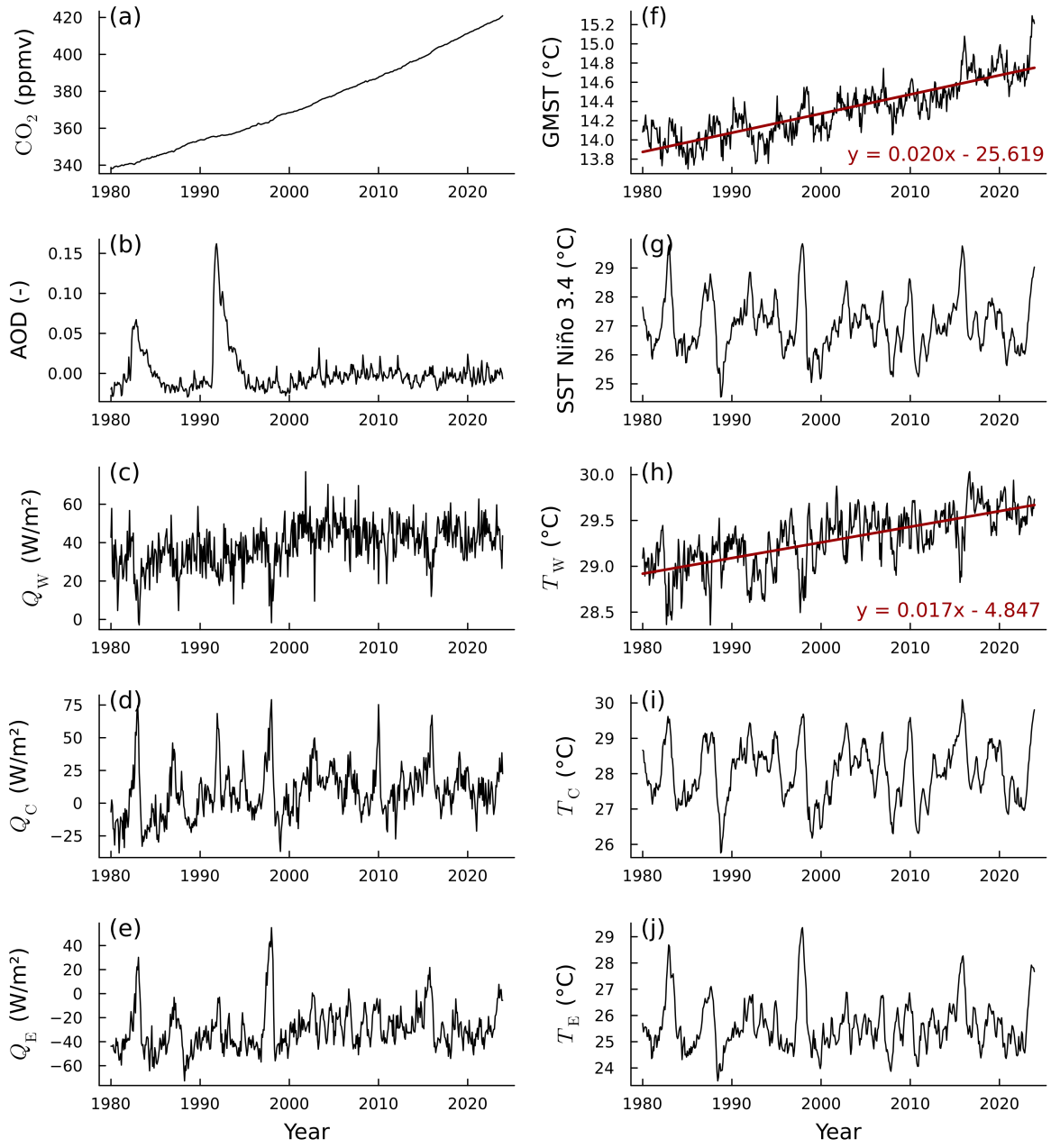

Figure 1: Time series of data used in this study. (a) Mean trend of global average marine surface CO_2 concentrations. (b) Global mean aerosol optical depth (AOD) anomaly. (c-e) Deseasonalized energy flux convergence Q into the atmosphere taking into account short- and long-wave radiation at the top of the atmosphere and the surface, as well as sensible and latent heat fluxes (Equation (1)). Q is defined positive into the atmosphere and is averaged over the western (Q_{W}), central (Q_{C}) and eastern (Q_{E}) Pacific. (f) Deseasonalized global mean surface temperature (GMST). (g) Deseasonalized sea surface temperatures in the Niño 3.4 region. (h-j) Deseasonalized sea surface temperatures in the western (T_{W}), central (T_{C}) and eastern (T_{E}) Pacific. The red line in (f, h) is a linear fit used to model the dependence of T_{r} on GMST in Equation (8). The linear expression can be found at the bottom right of the respective plot, where x represents the time in years A.D and y is the resulting temperature in °C.

For outgoing long-wave radiation, the net top of atmosphere long-wave radiation flux was averaged globally. For the net flux convergence into the atmosphere Q, the net top of atmosphere (TOA) and surface (S) long- (LW) and short-wave (SW) radiation fluxes as well as sensible (SHF) and latent (LHF) heat fluxes were considered:

$$Q_i = \mathrm{SHF}_i + \mathrm{LHF}_i + (\mathrm{SW}_i^{\mathrm{TOA}} - \mathrm{SW}_i^{\mathrm{S}}) + (\mathrm{LW}_i^{\mathrm{TOA}} - \mathrm{LW}_i^{\mathrm{S}}). \tag{1}$$

Here, i denotes the regions WP, CP and EP. The signs were chosen such that Q is positive for fluxes into the atmosphere, whereas the used fluxes from ERA5 are defined as positive towards the surface. All ERA5 data averages are latitude-weighted and were deseasonalized by removing the period's climatology but keeping the mean. For an estimate of ocean surface areas of the different regions, the area of available SST grids was considered.

For analysis of GMST response to Niño 3.4 from observations in Section 5.3, the SST in the Niño 3.4 region and GMST was converted to anomalies by subtracting a running mean of 30 years for Niño 3.4 and 15 years for GMST. The chosen periods are intended to be long enough to represent the climate well, but short enough to remove long-term trends, especially present in GMST (see Figure 1f). Subsequently, both time series were filtered using a 5-month running mean to remove high-frequency variability.

For calculating the heat capacity's equivalent ocean depth in Section 3.2, we assumed a specific heat capacity of 1004 J/kg/K for the atmosphere and 4184 J/kg/K for water (Thermtest, n.d.). To calculate the atmosphere area density, we applied a gravitational acceleration of $g = 9.81\,\mathrm{m\,s^{-2}}$ and a standard atmosphere pressure of $p = 10^5$ Pa. The density of surface ocean water was assumed to be $1025\,\mathrm{kg/m^3}$.

3 A Conceptual Full-Field Coupled ENSO-GMST Model

To capture the two-way interaction between ENSO and GMST, a comprehensive model representing both components is required. In this work, this is achieved by coupling a model for ENSO with a model for GMST. For the former, we build on a previously developed conceptual ENSO model from Fang et al. (2024) which is outlined in the next subsection. Thereafter, a simple energy-balance model for GMST is introduced, and the two models are coupled through key variables. A schematic overview of the coupled model is given in Figure 2.

3.1 A Three-Box ENSO Model

Theoretical ENSO frameworks aiming to explain the quasi-periodic behavior of the phenomenon are typically grouped into two approaches. One views the oscillation as a stable mode excited by high-frequency external forcing. Possible sources for this are the atmosphere through westerly wind bursts and the Madden–Julian oscillation (MJO) or the ocean by the means of tropical instability waves. The competing approach is the idea of ENSO as a self-sustaining oscillator that has a positive ocean-atmosphere coupling in form of the Bjerknes feedback and different proposed negative feedback mechanisms (Wang, 2018). The latter approach has the advantage that it does not rely on statistical noise and is hence completely deterministic. Nevertheless, through nonlinearities, these models are capable of reproducing complex dynamical features of ENSO. For example, Timmermann et al. (2003) were able to reproduce El Niño bursting behavior with a simple two-box model based on the model from Zebiak and Cane (1987) and the recharge oscillator paradigm (Jin, 1997).

The conceptual ENSO model from Fang et al. (2024) used in this study is a derivative of this idea and features three regions, representing the western, eastern and - as an extension to Timmermann et al. (2003) - the central Pacific (Figure 2b). The complete equation set features four equations for four prognostic variables with respect to time t. These variables are the SSTs T_{W}, T_{C} and T_{E} in the three regions WP, CP and EP, respectively and the thermocline depth h_{W} in the WP:

$$\frac{\mathrm{d}T_\mathrm{W}}{\mathrm{d}t} = -\alpha\left(T_\mathrm{W} - T_\mathrm{r}\right) - \frac{\epsilon\mu}{5}\left(T_\mathrm{C} - T_\mathrm{W}\right)^2, \tag{2a}$$

$$\frac{\mathrm{d}T_\mathrm{C}}{\mathrm{d}t} = -\alpha\left(T_\mathrm{C} - T_\mathrm{r}\right) - \epsilon\mu\left(T_\mathrm{E} - T_\mathrm{W}\right)^2 + \zeta\mu\left(T_\mathrm{C} - T_\mathrm{W}\right)\mathcal{H}\left(\mu\left(T_\mathrm{W} - T_\mathrm{C}\right)\right)\left(T_\mathrm{C} - T_\mathrm{sub}^\mathrm{C}\right), \tag{2b}$$

$$\frac{\mathrm{d}T_\mathrm{E}}{\mathrm{d}t} = -\alpha\left(T_\mathrm{E} - T_\mathrm{r}\right) + \zeta\mu\left(T_\mathrm{E} - T_\mathrm{W}\right)\mathcal{H}\left(\mu\left(T_\mathrm{W} - T_\mathrm{E}\right)\right)\left(T_\mathrm{E} - T_\mathrm{sub}^\mathrm{E}\right), \tag{2c}$$

$$\frac{\mathrm{d}h_\mathrm{W}}{\mathrm{d}t} = r\left(-h_\mathrm{W} - \frac{\eta}{2}\left(T_\mathrm{E} - T_\mathrm{W}\right)\right). \tag{2d}$$

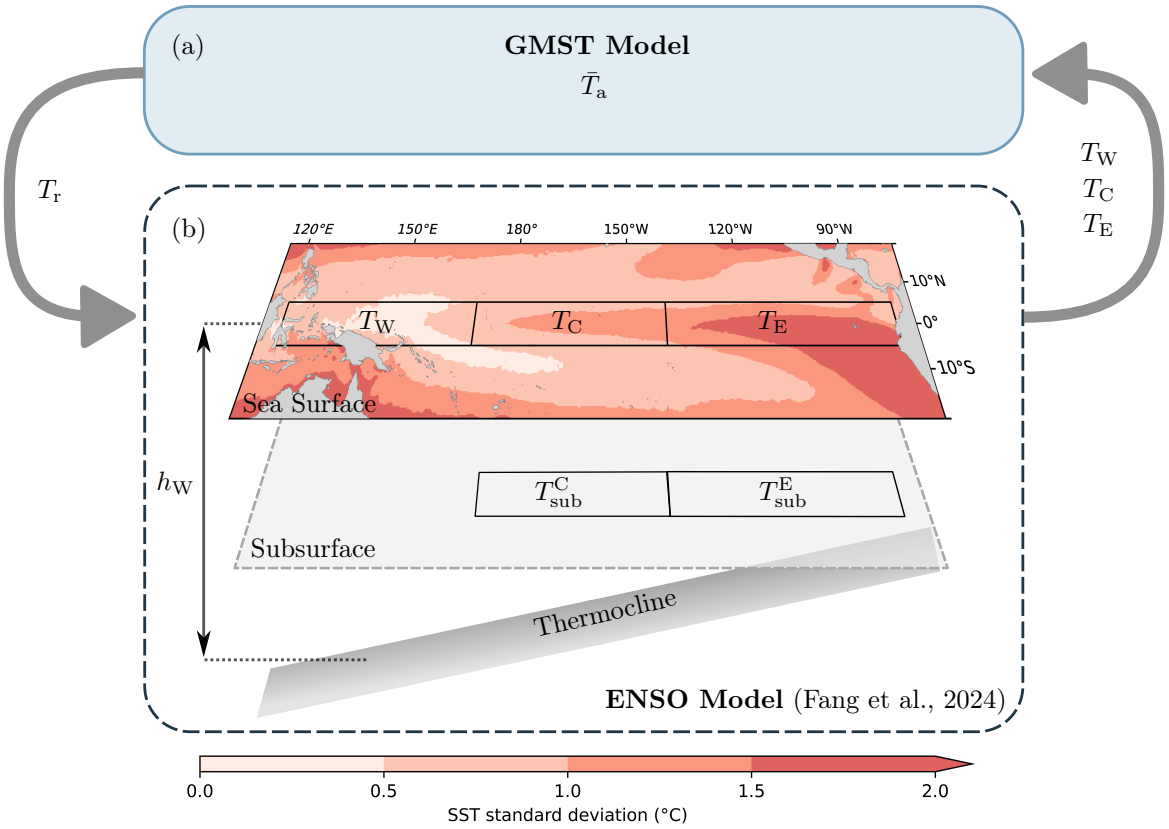

Figure 2: Schematic overview of the coupled ENSO-GMST model. (a) GMST model developed in this study with GMST ($\bar{T}_\mathrm{a}$) as the prognostic variable. (b) ENSO model from Fang et al. (2024). The three Pacific regions are marked, with their zonal extent of 120 °E - 170 °E and 170 °E - 150 °W, 140 °W - 80 °W for the western Pacific, central Pacific and eastern Pacific, respectively. The corresponding prognostic variables are western (T_W), central (T_C) and eastern (T_E) Pacific SSTs, and the thermocline depth anomaly in the western Pacific (h_W). The subsurface temperatures in the central ($T_\mathrm{sub}^\mathrm{C}$) and eastern ($T_\mathrm{sub}^\mathrm{E}$) Pacific are diagnostic variables. The models are connected through a coupling of key variables. The GMST model takes the SSTs of the three equatorial Pacific regions as input (top right arrow). GMST governs the radiative-convective equilibrium temperature T_r of the ENSO model (top left arrow). The sea surface shading indicates SST variability. Modified and extended from Fang et al. (2024).

In (2a) - (2c), the first term on the right-hand side (RHS) of the equations is a linear relaxation towards the radiative-convective equilibrium (RCE) temperature T_r with a thermal damping timescale of α^{-1}. This is referred to as Newtonian cooling and represents processes like horizontal mixing and energy fluxes to the atmosphere (Dijkstra, 2005).

Important ENSO-related feedbacks of zonal advection, upwelling and the thermocline are controlled by SST gradient-related wind stresses representing the Walker circulation. Consequently, various SST differences appear in the respective terms of the equations in connection with the dynamical coupling coefficient μ that measures the ability of SST differences to drive the wind stress.

The second term on the RHS of Equations (2a) and (2b) represents the advection feedback, which is proportional to the above-mentioned wind stress and the heat transported. The latter is itself linear in the temperature gradient, leading to the quadratic formulation. This feedback is governed by the zonal advection efficiency ϵ which is assumed to be 80 % lower in the central-western Pacific (Equation (2a)) due to the weaker coupling in this region (Fang et al., 2024).

Similarly, the third term on the RHS of (2b) and the second term of (2c) represent the upwelling feedback. As this feedback originates from Ekman pumping, the corresponding vertical velocity is controlled by the zonal wind stress which, as before, is driven by the temperature difference between the boxes. Since no downwelling is considered in this model, the Heaviside function $\mathcal{H}$ is included, which translates any negative Ekman pumping effects of westerly winds to zero. The upwelling heat transport is governed by the vertical upwelling efficiency ζ and is linear in the temperature difference between the surface and the subsurface as advective heat fluxes are assumed to dominate over diffusive processes (Dijkstra, 2005). The corresponding subsurface temperatures for the central and eastern Pacific, $T^\mathrm{C}_\mathrm{sub}$ and $T^\mathrm{E}_\mathrm{sub}$, respectively, are formulated as diagnostic equations

$$T^\mathrm{C}_\mathrm{sub} = T_\mathrm{r} - \frac{T_\mathrm{r} - T_\mathrm{r0}}{2}\left(1 - \tanh\left(\frac{H + h_\mathrm{C} - z_0}{h^*}\right)\right), \tag{3a}$$

$$T^\mathrm{E}_\mathrm{sub} = T_\mathrm{r} - \frac{T_\mathrm{r} - T_\mathrm{r0}}{2}\left(1 - \tanh\left(\frac{H + h_\mathrm{E} - z_0}{h^*}\right)\right). \tag{3b}$$

It is evident that the subsurface temperatures are governed by the RCE temperature T_r and the characteristic temperature at the thermocline depth T_r0. At the same time, the equations represent the strong non-linear dependence of a typical vertical temperature profile in the tropical Pacific on the thermocline depth (Jin, 1996). This mimics the canonical thermocline feedback where a shallow (deep) thermocline implies cooler (warmer) subsurface temperatures. In Equation (3), z_0 represents the depth at which the vertical velocity takes its characteristic value, h^* parametrizes the sharpness of the thermocline and H is the reference depth of the EP thermocline. Deviations from the latter are measured by the thermocline depth anomalies h_W, h_C and h_E in the WP, CP and EP, respectively. An equation for former is part of the prognostic set of equations in (2d) with a formulation equivalent to that in Jin (1997). Here, the dynamical adjustment timescale r^{-1} controls damping due to mixing and meridional energy loss, as well as the basin-wide wind-driven Sverdrup transport characterized by $\eta = \mu b L/\beta$. In the latter, b is the wind efficiency in driving the thermocline tilt, L is the basin width and β is the latitudinal derivative of the Coriolis parameter describing the beta plane. It is through this Equation (2d) that the model discharges and recharges heat that is available in the subsurface and thus provides negative feedback to the model. The thermocline in the CP and EP are a result of the assumption of a linear thermocline along the equator where the west-minus-east thermocline contrast is determined by the pressure gradient accompanying the equatorial winds (Timmermann et al., 2003), and h_C is the average between h_W and h_E

$$h_{\mathrm{C}} = h_{\mathrm{W}} + \frac{\eta}{2}\left(T_{\mathrm{E}} - T_{\mathrm{W}}\right), \tag{4a}$$

$$h_{\mathrm{E}} = h_{\mathrm{W}} + \eta\left(T_{\mathrm{E}} - T_{\mathrm{W}}\right). \tag{4b}$$

Equations (2d) and (4) demonstrate that a stronger easterly wind induces a deeper thermocline depth in the WP but also leads to a steeper thermocline slope affecting the CP and EP.

In summary, the ENSO model used in this study is a three box self-sustained non-linear conceptual model from Fang et al. (2024) that reproduces some of the rich dynamical behavior of ENSO without any external forcing required. The set of equations in (2), (3) and (4) include important positive ENSO feedbacks, namely the zonal advection, upwelling as well as the thermocline feedback, and the recharge-discharge paradigm from Jin (1997). A more comprehensive model description can be found in Fang et al. (2024).

In this study, unless otherwise noted, we use the following parameter values where, for $T_{\mathrm{r}} = 29\,^{\circ}\mathrm{C}$, the model shows limit-cycle oscillations in an "observed regime" (Fang et al., 2024): $T_{\mathrm{r0}} = 20\,^{\circ}\mathrm{C}, \alpha^{-1} = 180\,\mathrm{day}, r^{-1} = 400\,\mathrm{day}$, $H = 100\,\mathrm{m}$, $z_0 = 75\,\mathrm{m}$, $h^* = 62\,\mathrm{m}$, $\mu = 0.0026\,\mathrm{K}^{-1}\,\mathrm{day}^{-1}$, $\eta = 22\,\mathrm{m\,K}^{-1}$, $\epsilon = 0.6$, $\zeta = 1.85$.

3.2 A Simple Model for Pacific Influence on GMST

This section presents the simple full-field GMST model developed in this work. We begin by outlining the basic model structure, followed by a detailed explanation of the model parameters and their quantification. The section concludes with a discussion on parameter estimation, comparing the results to existing literature and observational data.

3.2.1 Model Formulation

Motivated by previous work from Hu and Fedorov (2017), Thompson et al. (2009) and Yulaeva and Wallace (1994), who developed simple anomaly models for the atmospheric response to ENSO, we propose a full-field GMST model tailored to the previously discussed ENSO model from Fang et al. (2024). The GMST model represents a 1-layer atmosphere. It is based on a global energy balance and is able to dynamically adjust to SST changes in the three equatorial Pacific regions, the WP, CP and EP. The model is formulated as a first-order differential equation for GMST, which is denoted as $\bar{T}_{\mathrm{a}}$ as it describes the mean atmospheric temperature in our model. It incorporating the primary factors that influence it from a perspective of thermodynamics:

$$C\frac{\mathrm{d}\bar{T}_{\mathrm{a}}}{\mathrm{d}t} = \mu_{\mathrm{oa}}\left(\frac{S_W}{S}T_{\mathrm{W}} + \frac{S_C}{S}T_{\mathrm{C}} + \frac{S_E}{S}T_{\mathrm{E}} - \frac{S_P}{S}\bar{T}_{\mathrm{a}}\right) + \mathrm{OLR}(\bar{T}_{\mathrm{a}}, \mathrm{CO}_2) + F(I). \tag{5}$$

Here, C is the effective model heat capacity per unit area, S_i/S are the surface areas of the western ($i = \mathrm{W}$), central ($i = \mathrm{C}$) and eastern ($i = \mathrm{E}$) Pacific and whole tropical Pacific ($i = \mathrm{P}$ with $S_{\mathrm{P}} = S_{\mathrm{W}} + S_{\mathrm{C}} + S_{\mathrm{E}}$), respectively, relative to the earth's total surface S. The first term of the RHS of Equation (5) represents the dynamic energy flux between the atmosphere and the tropical Pacific. This process is assumed to be linear in the temperature difference between the atmosphere and the sea surface, and is governed by the Pacific ocean-atmosphere exchange coefficient μ_{oa}. The system loses energy through outgoing long-wave radiation (OLR), which is a function of $\bar{T}_{\mathrm{a}}$ and CO_2 concentration. Energy is supplied to the atmosphere globally by $F(I)$, where I represents long-term means of absorbed incoming short-wave radiation, surface-atmosphere fluxes outside the tropical Pacific region and a reference energy exchange in the tropical Pacific region at zero temperature difference between sea surface and atmosphere.

Supported by multiple studies (e.g., Koll and Cronin (2018) and M. Cai et al. (2023)), OLR is assumed to be linear with GMST

$$\mathrm{OLR}(\bar{T}_\mathrm{a}, \mathrm{CO_2}) = m\bar{T}_\mathrm{a} + n - a \log_2 \frac{\mathrm{CO_2}}{\mathrm{CO_{2,ref}}}, \tag{6}$$

where m is the slope and n is the y-intercept of the linear relationship. To explicitly resolve the influence of anthropogenic climate change, the rightmost term on the RHS of Equation (6) models the radiative forcing (RF) from changing $\mathrm{CO_2}$ concentration with respect to pre-industrial levels of $\mathrm{CO_{2,ref}} = 280\,\mathrm{ppm}$ (NOAA, 2022), reducing the total OLR. Consequently, a governs the RF per doubling of $\mathrm{CO_2}$ concentration. In the following, the methods and results of choosing appropriate values for the introduced parameters are presented.

3.2.2 Model Parameter Estimation

As dynamic heat exchange is only modelled between ocean and atmosphere in the tropical Pacific, the surface areas S_W, S_C and S_E represent the respective area covered by ocean. Estimates of these areas are gained by relating the ocean grid area from SST data within a region to earth's surface area, which yields the values summarized at the top of Table 1.

Employing reanalysis data for OLR, $\bar{T}_\mathrm{a}$ and $\mathrm{CO_2}$, the parameters in Equation (6) can be found by minimizing the root-mean-square error (RMSE) to $0.46\,\mathrm{W\,m^{-2}}$. The resulting parameters including their uncertainty from the fit are available in Table 1.

With the parameterization of OLR concluded, the missing parameters from Equation (5), namely the heat capacity C, the equatorial Pacific ocean-atmosphere coupling coefficient μ_oa and the fixed net energy influx I can be found by again minimizing RMSE with respect to observations. To account for radiative effects from major volcanic eruptions such as El Chichón in 1982 or Pinatubo in 1991 (Global Volcanism Program, 2024), we use a term proportional to the AOD anomaly, similar to Hu and Fedorov (2017), during the fitting process

$$F(I) = \begin{cases} I + b\mathrm{AOD} & \text{for fitting,} \\ I & \text{for model use.} \end{cases} \tag{7}$$

Evidently, this AOD term is omitted when the model is used later on, assuming a climate without major eruptions. For the fitting, data of $\bar{T}_\mathrm{a}$, $\mathrm{CO_2}$, AOD, and SST in the three Pacific regions was used. The model was integrated using the Euler method with a time-step of one month, and GMST of January 1980 as initial condition. Optimized model parameters are found in Table 1. The given uncertainty represents the combined uncertainty originating from the standard error of the fit and the uncertainty from the parameterization of OLR (Equation (6)). The latter was estimated by employing a Monte Carlo simulation with 500 samples assuming a multivariate normal distribution for the uncertainty of parameters in Equation (6). Including this uncertainty propagation roughly doubled each value in the covariance matrix of the parameters with respect to the covariance matrix from the fit, implying high sensitivity on the OLR parameters. In fact, strong correlations exist. For instance, a higher slope m of OLR increases the ocean-atmosphere coupling μ_oa, as the system needs to compensate for the increased energy loss.

The optimized model is able to reproduce general features of GMST variability with a RMSE of $0.12\,^\circ\mathrm{C}$ which can be seen in Figure 3. The RMSE is significantly bigger than in Hu and Fedorov (2017), largely due to the fact that the employed monthly instead of annual data includes strong high frequency variability of the atmosphere not captured by our model.

Table 1: Optimized parameters for the GMST model Equation (5) with OLR from Equation (6). Note that $F(I)$ during fitting is different from $F(I)$ during model use, where $b = 0$ as no volcanic influence is assumed (see Equation (7)). The relative ocean surface area S_i/S is assumed to have negligible uncertainty compared to other parameters. The uncertainty of m, n and a are the uncertainties of the fit. The uncertainties for a, C, μ_{oa}, I and b result from both the fit's uncertainty and the uncertainty in the OLR parameterization, estimated using a Monte Carlo simulation with 500 samples.

Parameter	Unit	Description	Value
S_{W}/S	%	Relative ocean surface area WP	1.10
S_{C}/S	%	Relative ocean surface area CP	1.21
S_{E}/S	%	Relative ocean surface area EP	1.45
m	$\mathrm{W\,m^{-2}\,K^{-1}}$	Slope of OLR	1.59 ± 0.14
n	$\mathrm{W\,m^{-2}}$	Offset of OLR	-212.40 ± 38.80
a	$\mathrm{W\,m^{-2}}$	RF per CO_2 doubling	4.59 ± 0.44
C	$\mathrm{10^7\,J\,m^{-2}\,K^{-1}}$	Effective model heat capacity	2.39 ± 0.40
μ_{oa}	$\mathrm{W\,m^{-2}\,K^{-1}}$	Equatorial Pacific ocean-atmosphere coupling	9.79 ± 1.26
I	$\mathrm{W\,m^{-2}}$	Constant energy influx	237.62 ± 0.62
b	$\mathrm{W\,m^{-2}}$	Slope for AOD influence, only used for fitting	-4.34 ± 0.64

3.2.3 Model Parameter Validation

Our GMST model resembles the model from Hu and Fedorov (2017) with some notable differences. Setting aside the disparities in zonal extent of the Pacific regions and the shorter timescale of our model, the biggest difference lies in the physical interpretability. Our model offers a full-field representation of GMST responses to ENSO by employing explicit parameterization of OLR, the equatorial Pacific ocean-atmosphere coupling through μ_{oa} and the delayed atmosphere response due to the effective heat capacity C. This allows us to explicitly compare the parameters to literature and assess physical validity which is discussed thoroughly in the following paragraphs.

The linear fit for the OLR radiation yields similar values as used in North (1975), but a weaker slope than that found in Koll and Cronin (2018) and M. Cai et al. (2023). The discrepancy is likely caused by the explicit parameterization of carbon dioxide RF, and the fact that we use globally averaged surface temperature data instead of local surface temperatures as in Koll and Cronin (2018) and M. Cai et al. (2023).

The RF per doubling of CO_2, $a = (4.59 \pm 0.44)\,\mathrm{W\,m^{-2}}$, is in agreement with estimates from CO_2 doubling experiments that find an effective radiative forcing (ERF) of $(3.93 \pm 0.48)\,\mathrm{W\,m^{-2}}$ (Smith et al., 2018; IPCC, 2023, Table 7.2), if uncertainties are taken into account. Similarly, Weaver et al. (2001) use a specified radiative forcing of $4\,\mathrm{W\,m^{-2}}$ for their earth system model. Other greenhouse gases such as methane and nitrous oxide that are not explicitly considered in our model and have therefore possibly contributed to the higher estimate of a. When equatorial Pacific SSTs are held at their historic mean, this translates to a model climate sensitivity of 2.3 °C, which is close to the sensitivity of the model from Hu and Fedorov (2017). As our model is trained on a transitional period with increasing CO_2 concentration, its climate sensitivity can be compared to the transient climate sensitivity, for which the Intergovernmental Panel on Climate Change (IPCC) assesses a very likely range of 1.2 °C to 2.4 °C (IPCC, 2023, Table 7.14).

The model's effective heat capacity C is equivalent to that of the atmosphere combined with the uppermost $\sim 3.8\,\mathrm{m}$ of the ocean, implying that ENSO related changes of GMST also impact the ocean surface layer. This is somewhere between the values found in Thompson et al. (2009) ($\sim 2\,\mathrm{m}$) and Yulaeva and Wallace (1994) ($\sim 10\,\mathrm{m}$), who conducted similar experiments.

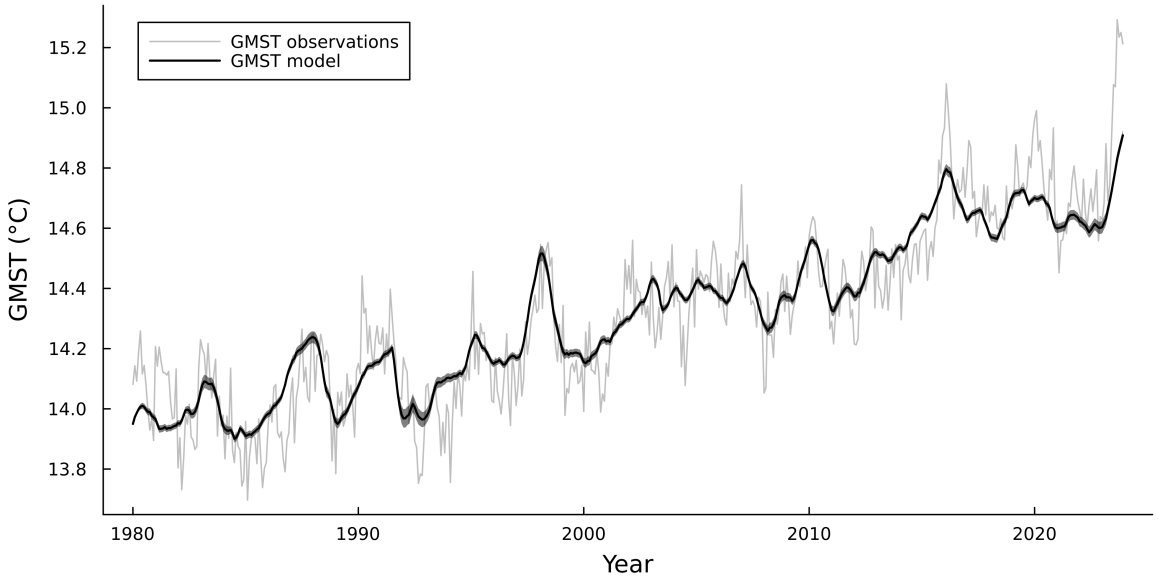

Figure 3: Time series for GMST from reanalysis (gray) and GMST model output (black) with optimized parameters from Table 1. The modeled GMST spread induced by the parameter uncertainty is indicated by the gray ribbon which marks the standard deviation from a Monte Carlo simulation with 500 samples. However, due to the small spread, the gray ribbon aligns closely with the black line. The RMSE of the fit is 0.12 °C.

Although not describing the exact same quantity, the constant energy influx $I = (237.5 \pm 0.7)\,\mathrm{W\,m^{-2}}$ into the atmosphere can be compared to the global energy influx into the atmosphere per unit area. The IPCC estimates this flux to be $239\,\mathrm{W\,m^{-2}}$ for the climatic conditions of the 21st century (IPCC, 2023, Fig. 7.2), which is very close to the value of I used in our model.

For the ocean-atmosphere exchange coefficient $\mu_{\mathrm{oa}} = (9.8 \pm 1.3)\,\mathrm{W\,m^{-2}\,K^{-1}}$, there exists a wide parameter range in literature. Our value agrees very well with that used in Thompson et al. (2009) ($10\,\mathrm{W\,m^{-2}\,K^{-1}}$) but is much lower than that in Yulaeva and Wallace (1994) ($25\,\mathrm{W\,m^{-2}\,K^{-1}}$). Reanalysis flux data implies a coupling of $\mu_{\mathrm{oa}} = (17.5 \pm 0.2)\,\mathrm{W\,m^{-2}\,K^{-1}}$ across the equatorial Pacific basin (Figure 4), right in the middle of the literature range. A possible explanation for the discrepancy is that μ_{oa} in our model is sensitive to other model parameters and measures global net energy exchange while μ_{oa} derived from flux data only takes into account local energy fluxes.

With the GMST model set up and the required parameters defined, the next step is the coupling of the ENSO model to the GMST model, described in the following section.

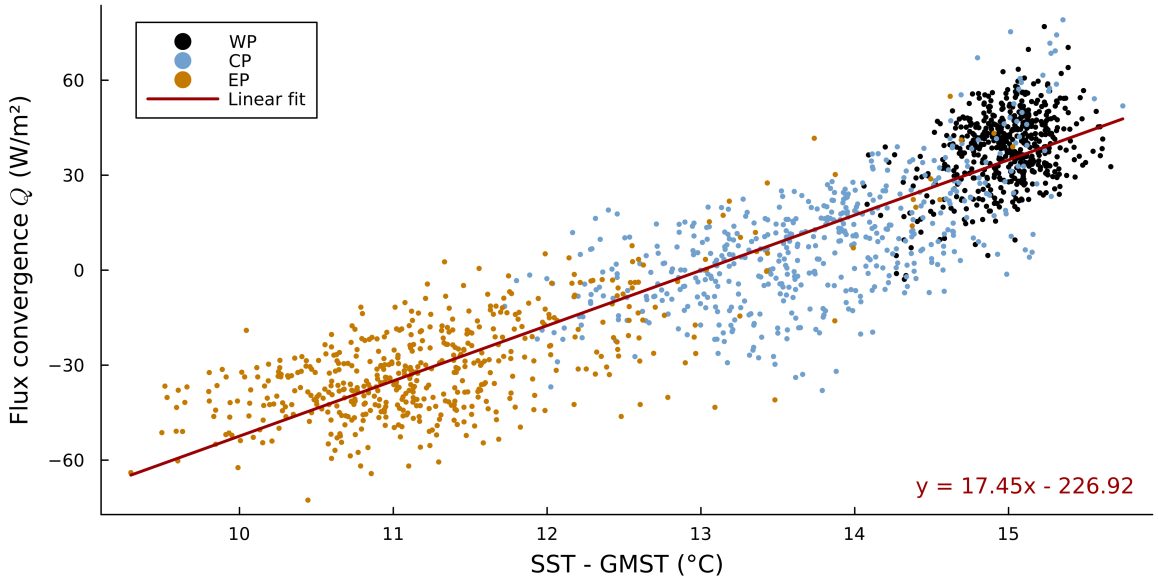

Figure 4: Energy flux convergence Q, defined as positive into the atmosphere, as a function of temperature difference between local SSTs and GMST. Following Equation (1), Q includes net short- and long-wave radiation as well as sensible and latent heat fluxes. SSTs were averaged in the western (WP, black), central (CP, blue) and eastern (EP, orange) Pacific separately. The expression for the linear fit (red) can be found on the bottom right where y represents the flux convergence Q in $\mathrm{W\,m^{-2}}$ and x is the temperature difference in °C. The slope of the linear fit is $(17.45 \pm 0.20)\,\mathrm{W\,m^{-2}\,K^{-1}}$, where the uncertainty is the standard error of the fit.

3.3 Two-Way Model Coupling

To gain a comprehensive understanding of the interdependence of GMST and ENSO, the ENSO model and the GMST model are coupled in two directions. Coupling GMST to respond to ENSO is achieved by using the SST output of the WP, CP and EP from the ENSO model as input for the GMST model.

Quantifying the influence GMST has on ENSO is much less straight-forward and ENSO responses to anthropogenic climate change are not fully understood (W. Cai et al., 2021). Furthermore, some projected changes such as the weakening of the trade winds and the enhanced warming of the eastern Pacific are not yet supported by observations, potentially due to masking by low frequency variability (W. Cai et al., 2015). Other mechanisms such as the faster warming of the surface than the deep ocean and the shoaling thermocline (Collins et al., 2010) are more certain, but it is difficult to pinpoint the causality. Consequently, numerous parameters in the ENSO model in Equations (2), (3) and (4) are potentially influenced by GMST. In this study we limit ourselves to the adjustment of RCE temperature T_r. RCE is a simple paradigm usually used for the atmosphere (Jakob et al., 2019) that describes a balance between radiation and surface heat fluxes and has been applied to the equatorial Pacific in the ENSO model. Typically, due to its strong regulation (Sun, 2000) and the vast energy required for a perturbation (Newell, 1986; Newell & Dopplick, 1979), this temperature is fixed at approximately $29-29.5\,°\mathrm{C}$ (Fang et al., 2024; Sun, 2000; Timmermann et al., 2003). However, with significant greenhouse gas forcing, the supplied energy may be sufficient to change RCE and, as a first order approximation, we assume a linear response of T_r to GMST

$$T_\mathrm{r} = A\bar{T}_\mathrm{a} + B. \tag{8}$$

To find the parameters A and B, we assume that SSTs in the warm pool - with its high average temperatures of around 29.5 °C (Figure 1h) and low variability (Figure 2b) - is a useful proxy for T_r. This is also consistent with our ENSO model, where the western Pacific temperature T_W is dominated by T_r as the advection is very weak (see Equation (2a)). To extract only long-term trends in the relationship of T_W and GMST, a linear model was first fit to both GMST and T_W time series (orange line in Figure 1f,h). From that, $A = (0.85 \pm 0.05)\,\mathrm{K\,K^{-1}}$ and $B = (56.7 \pm 13.1)\,\mathrm{K}$ can be found by eliminating the time-dependence. The uncertainty was estimated by propagating the uncertainties from the two linear fits.

This 2-step linear fitting procedure extracts the long-term relationship between GMST and T_W, while allowing an estimation of uncertainty from the fit. Alternatively, the parameters can also be found through a direct linear fit between GMST and T_W. To remove variability up to interannual timescales, 4th order Butterworth 8 years low-pass filter was applied to both GMST and T_W before the fit. This results in a correlation of over 0.97 with a slope of $A = 0.86\,\mathrm{K\,K^{-1}}$ when minimizing the RMSE in T_W direction to 0.05 °C. A similar result of $A = 0.88\,\mathrm{K\,K^{-1}}$ is found when a Deeming regression with an assumed uncertainty of 0.1 °C is applied. This underpins the robustness of the linear relationship between GMST and T_W found before. However, as the low-pass filter removes information important for uncertainty estimation, we stick to the results of the 2-step linear fitting procedure of the previous paragraph for the following analysis.

With that, we have constructed a full-field two-way coupled conceptual ENSO-GMST model. In the next section, we will explore how this model was used to investigate the interplay between ENSO and GMST.

4 Methodology

With the coupled ENSO-GMST Model set up and model parameters found, the model can be used to investigate its behavior in a changing climate, i.e., under different CO_2 concentrations. For our simulation, we integrated the model over 400 years with a time step of 1 day employing a 4th order Runge-Kutta method. The numerical integration was performed in *Julia* (Bezanson et al., 2017) using *DifferentialEquations.jl* (Rackauckas & Nie, 2017). Bifurcation analysis was carried out utilizing *Bifurcationkit.jl* (Veltz, 2020). As initial conditions, observational mean values of GMST = 14.31 °C, $T_\mathrm{W} = 29.29$ °C, $T_\mathrm{C} = 28.05$ °C and $T_\mathrm{E} = 25.60$ °C are used. For the WP thermocline depth anomaly, we use $h_\mathrm{W} = 30$ m initially. An analysis with randomized initial conditions revealed that the solution characteristics are however not sensitive to the exact initial conditions chosen. Only once the initial conditions deviate too far from physically realistic values, the oscillation seizes, and the solution stays constant in time. The first 100 years of the solution were omitted in the subsequent analysis to ensure the model has fully spun up. The integration procedure was repeated for CO_2 concentrations between 100 ppmv and 800 ppmv. Using best estimate (BE) parameters from Table 1, the model was integrated repeatedly, each time increasing CO_2 concentration in steps of 1 ppmv. For a more comprehensive analysis that also takes the parameter uncertainty into account, we also employed a Monte Carlo (MC) simulation with 500 samples and CO_2 steps of 5 ppmv. In the MC approach, parameters were drawn randomly from a multivariate normal distribution generated by the covariance matrix of the parameters. The projected distribution is depicted in Figure 5.

To obtain the model mean state in Subsection 5.1, at each CO_2 level, the time series of each prognostic variable was averaged over the available period. For periodic orbits, this introduces a slight error as the averaging period is not necessarily an integer of full periods. However, this error is expected to be negligible due to the long averaging period with respect to the typical ENSO period. Advantageously, this method stays well-defined even for chaotic model behavior, which the coupled model inherits from the ENSO model and is briefly discussed in Subsection 5.2. The averaging was repeated for each individual MC simulation yielding N simulation means (sim-means). The MC mean and its uncertainty are then calculated as the mean and standard deviation of these sim-means.

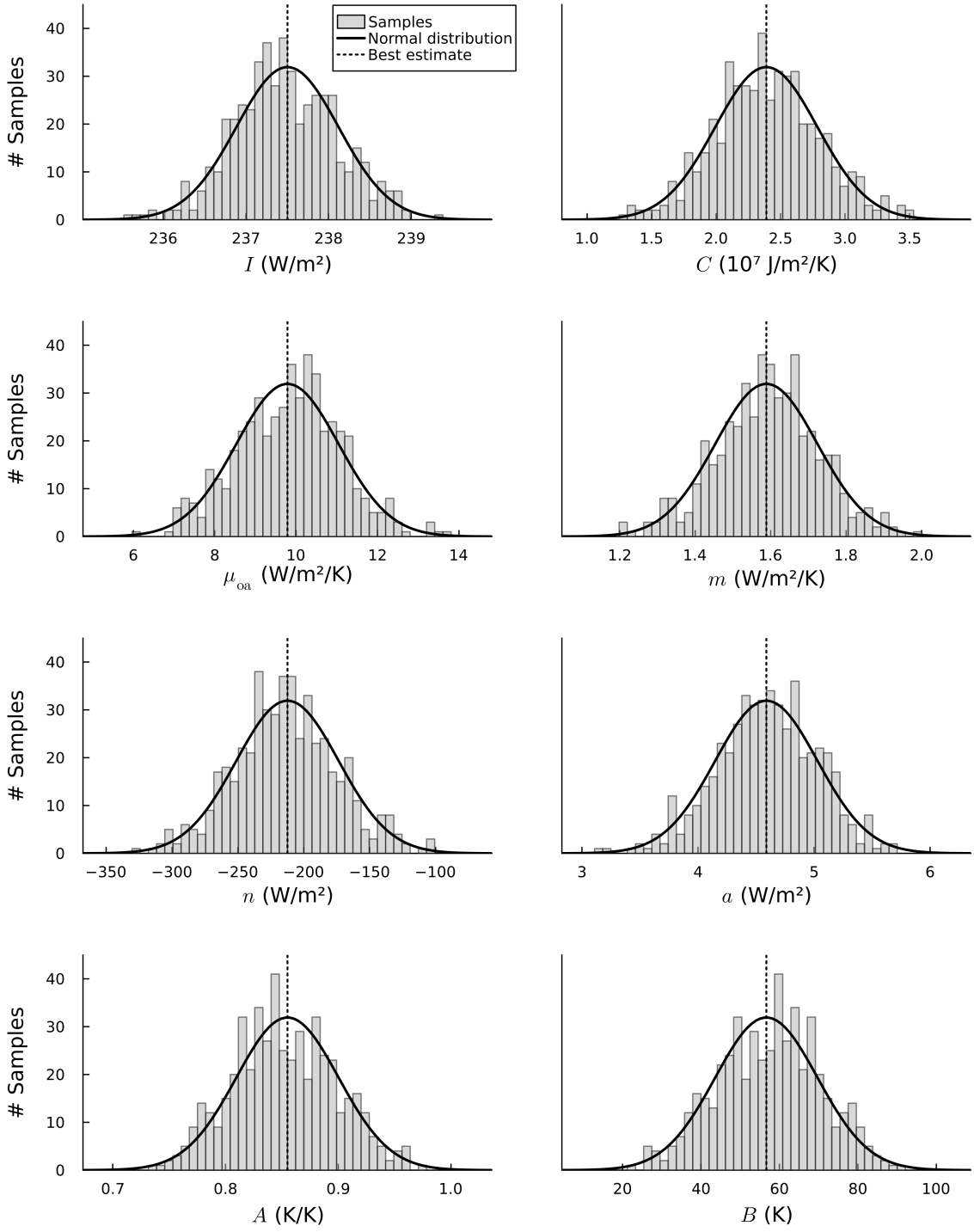

Figure 5: Sample distribution of GMST model and coupling parameters drawn from a multivariate normal distribution (projection in black) for the Monte Carlo simulation with a total of $N = 500$ samples. The best estimate parameter is marked by the vertical dotted line.

To characterize El Niño in Subsection 5.2, the SST anomaly in the Niño 3.4 region, reflecting the Niño 3.4 index (Trenberth, 1997), is used. As the model does not directly simulate the temperature in this region, we used a weighted average of the SST in the CP and EP as a proxy. Anomalies were then calculated by subtracting the mean SST of that region. In each MC simulation at each CO_2 concentration, local maxima are identified using *Peaks.jl*. Following the definition of Trenberth (1997) for an El Niño, only the local maxima with a SST anomaly of $\geq 0.4\,°C$ are considered in the subsequent analysis. Note that the exact value of this threshold is arbitrary and does not significantly affect the results. The filtered local maxima of each MC simulation are used to calculate the mean (sim-mean) and maximum (sim-max) of the time series. Then, those values are used to get the MC mean by averaging all sim-means and the MC max by averaging all sim-maxs. To assess the uncertainty of MC mean and MC max, the standard deviation of the sim-means and sim-maxs, respectively, is used. An analogous procedure was employed to assess the period of ENSO. To extract the MC mean period, the time between two filtered local maxima is calculated and averaged, first over the time series of each MC simulation, then over all MC simulations. Additionally, to visualize the qualitative model behavior for one set of parameters, we also employ an orbit diagram (Strogatz, 2015) in Figure 10a. Here, for BE parameters, the identified local extrema are neither filtered nor averaged, but directly visualized in a scatter plot. Here, each point in the orbit diagram represents a local maximum and, consequently, negative values are also possible.

To quantify the response of GMST to ENSO in Subsection 5.3, we again exploit the Niño 3.4 index as a measure for ENSO. Assuming a linear relationship between Niño 3.4 index and GMST, we fit a regression line to the model data and extract the slope. Beforehand, the GMST time series was shifted in time such that the correlation between Niño 3.4 index and GMST is maximized. This accounts for the delayed response of GMST as a result of the model heat capacity C. The obtained time lag is what we refer to as the delay between ENSO and GMST. As before, the MC mean and its uncertainty are calculated by calculating the mean and standard deviation of the slopes of the individual MC simulations at each available CO_2 concentration. However, the regression line and the delay were only considered in the MC mean if the the respective MC simulation was in an oscillatory regime as determined by bifurcation analysis.

5 Model Results

This section presents an in-depth analysis of the model behavior across different climates, focusing on the mean state, the characteristics of ENSO and the response of GMST to ENSO.

5.1 Mean States in a Changing Climate

One of the key advantages of employing a full-field model is the ability to investigate changes in the mean state. Figure 6 shows the mean state of all prognostic variables in the coupled model, i.e., $\bar{T}_a$, T_W, T_C, T_E and h_W, as a function of CO_2 concentrations. Slight deviations of the MC mean (solid) and the equilibrium found by collocation (dash-dotted) are visible above 400 ppmv CO_2 concentrations, which presumably originate from secondary bifurcations, as discussed in Fang et al. (2024).

Our coupled model shows increasing GMST (green) which is a direct consequence of the radiative forcing term in Equation (6) controlled by the parameter a. With GMST, following Equation (8), RCE temperature T_r (dashed black) rises, too, albeit at a slower pace, as $A < 1$. With this, the WP SST experiences a similar increase, and the corresponding thermocline (dark blue) deepens. However, the other Pacific regions experience a weaker SST increase, and after around 450 ppmv even a decrease. This is counterintuitive as one might expect a stronger warming of the colder regions in the CP and EP as seen in GCMs (W. Cai et al., 2021). Therefore, leveraging the conceptual nature of our model, we investigate the physical mechanisms behind this behavior in the following paragraphs.

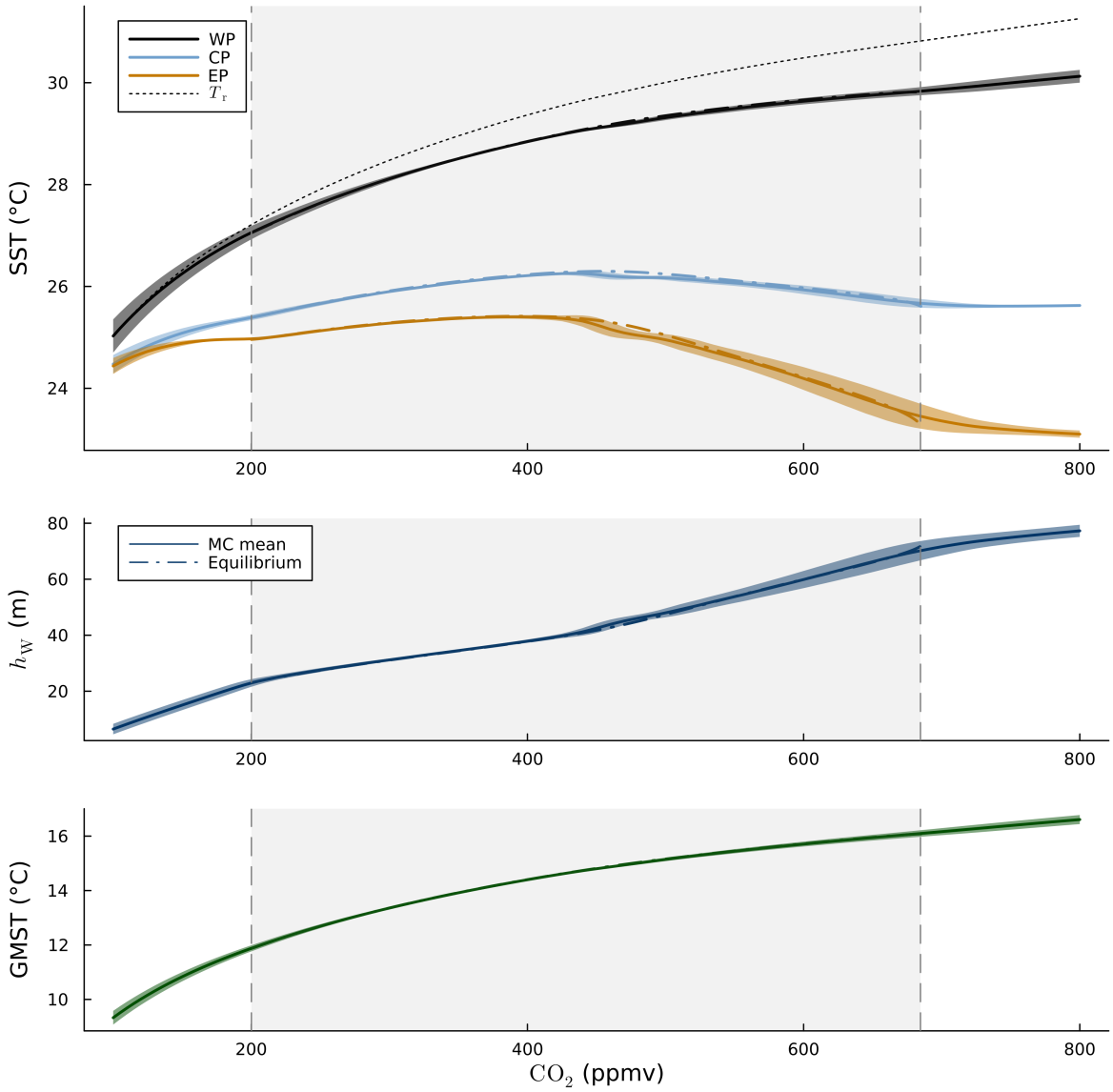

Figure 6: Mean states of prognostic variables of the coupled model, i.e., western (T_{W}), central (T_{C}) and eastern (T_{E}) Pacific SSTs, western thermocline depth anomaly (h_{W}) and GMST, as a function of CO_2 concentrations. The solid line represents the mean of the MC samples and the shaded band represents the corresponding standard deviation. The dash-dotted line is the equilibrium state of the model as determined by orthogonal collocation for BE parameters. The mean radiative convective equilibrium temperature T_{r} is represented by the black short dash line. The vertical dashed lines in gray indicate Hopf bifurcations for BE parameters, enclosing the gray shaded area where the model shows oscillatory behavior.

To understand CO_2 induced changes of the ENSO mean state, it is imperative to understand the dominating mechanisms acting on it. When a long-term average is applied to the variables in Equation (2), the time derivatives vanish which simplifies the expression for the WP thermocline anomaly and with that the thermocline anomalies in the CP and EP (Equation (4)), too, yielding

$$\langle h_{\mathrm{W}} \rangle = -\frac{\eta}{2} \left(\langle T_{\mathrm{E}} \rangle - \langle T_{\mathrm{W}} \rangle \right), \tag{9a}$$

$$\langle h_{\mathrm{C}} \rangle = 0, \tag{9b}$$

$$\langle h_{\mathrm{E}} \rangle = -\langle h_{\mathrm{W}} \rangle. \tag{9c}$$

Here, $\langle\rangle$ denotes time-averaging over a long period relative to oscillation period, which is implicitly understood throughout the following discussion. Consequently, the trade winds now deepen the WP thermocline and the EP thermocline is lifted by the same amount, with the CP thermocline remaining constant. This has direct consequences on the positive feedback loop of the ENSO model that acts to increase the zonal SST gradient in the mean state, with the working principle explored in Figure 7a. Ultimately, this feedback loop is constrained by a minimum subsurface temperature (T_{r0}) such that a balance with the Newtonian cooling term can be found.

Tracking the impacts on the zonal SST gradients in Figure 7a, a possible mechanism for its observed increase in a warmer climate is the subsurface temperature in the EP. In the following, we argue how increasing RCE temperature T_{r} initially cools the subsurface, acting as an entry point to the feedback mechanism.

The system of Equations (2) - (4) for the ENSO model exhibits translational invariance in temperature, which is a result of the fact that all temperature-related terms are expressed as differences. This implies that a constant shift ΔT in all temperature variables does not change the model dynamics. In fact, one can quickly verify that ΔT would cancel out in the equations. As a side effect, this also implies that the model works both in Kelvin and Celsius. As only the two parameters T_{r0} and T_{r} govern the unit of the temperature variables, translating them (for instance by adding ΔT) equates to a change in the frame of reference. Note that it is technically necessary that initial conditions are also adjusted with these two parameters. However, as the model is allowed to reach its dynamical equilibrium within the 100 years spin-up phase, this is not required as long as the changes are not too large. This change of reference helps to reformulate what it means to increase T_{r} in the model.

Let us assume a reference state with $T_{\mathrm{r0}} = T_{\mathrm{r0}}^0$ and $T_{\mathrm{r}} = T_{\mathrm{r}}^0$ (Figure 7b). Let ΔT_{r} be the induced change on T_{r} as a result of an increased GMST, such that $T_{\mathrm{r}}' = T_{\mathrm{r}}^0 + \Delta T_{\mathrm{r}}$ is the parameter after it's adjustment to a warmer climate. Next, performing a coordinate transformation by subtracting ΔT_{r} from T_{r}' and T_{r0}^0, yields

$$\tilde{T}_{\mathrm{r}} = T_{\mathrm{r}}^0, \tag{10a}$$

$$\tilde{T}_{\mathrm{r0}} = T_{\mathrm{r0}}^0 - \Delta T_{\mathrm{r}}. \tag{10b}$$

Here, $\tilde{T}_{\mathrm{r}}$ and $\tilde{T}_{\mathrm{r0}}$ define a new state after the impact of climate change and the coordinate transformation. This shows that a change of T_{r} is equivalent to the opposite change of T_{r0} (Figure 7b). Exploiting this symmetry, we can investigate the effect of an increasing T_{r} in Equations (2) - (4) by analyzing the impact of a decreasing T_{r0}. Under this perturbation, Equation (2) does not change directly, but is only affected by changes in the subsurface temperatures described in Equation (3). Here, as the hyperbolical tangent function is bounded by $(-1, 1)$, the subsurface temperatures would decrease as T_{r0} is decreasing. This yields the key result: *increasing T_r is dynamically equivalent to keeping T_r constant but lowering T_{r0} which acts to reduce the initial subsurface temperatures.*

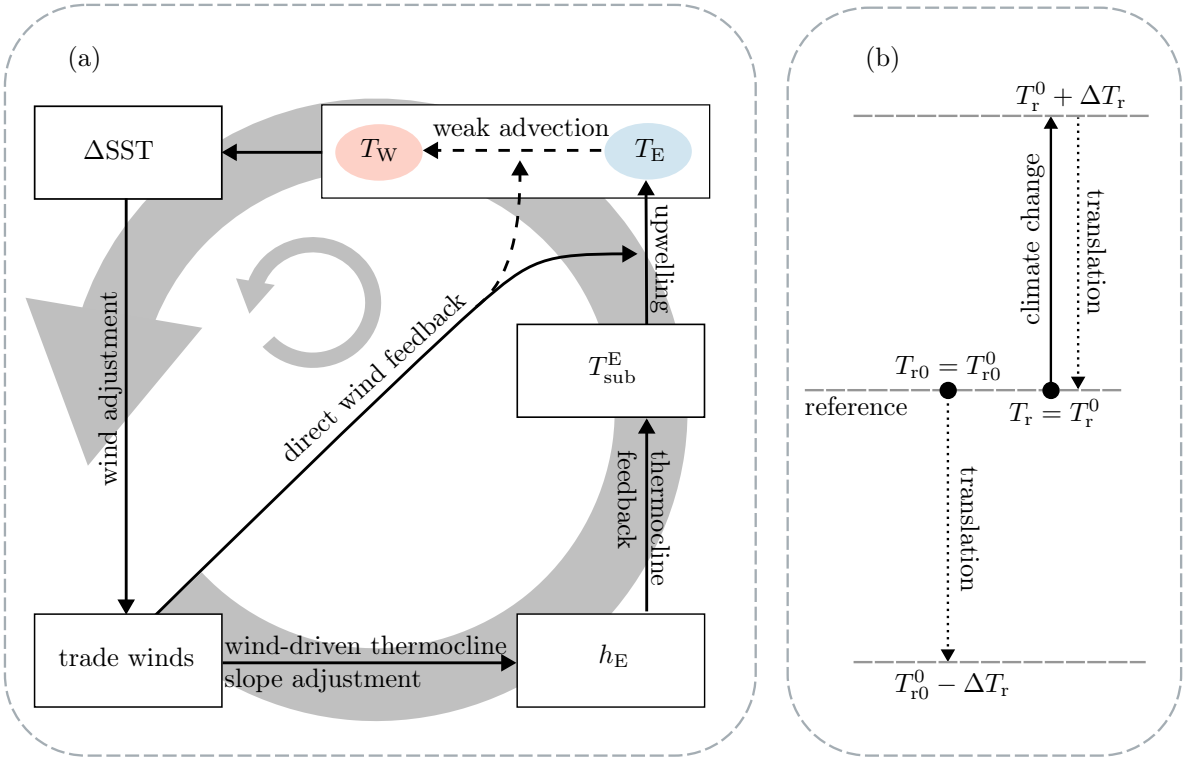

Figure 7: (a) Simplified positive feedback mechanism of the ENSO model mean state. A relative decrease of EP subsurface temperature $T^{\mathrm{E}}_{\mathrm{sub}}$ (mid right), caused for example by faster initial warming of the sea surface than the subsurface, cools down the EP SST T_{E} through upwelling. Due to the weak advection coupling of WP and EP, the WP SST T_{W} decreases, too, but at a lower magnitude (top right). This increases the zonal SST difference ΔSST (top left), which in turn strengthens the trade winds (bottom left). Following Equations (9), this increases the thermocline slope and consequently lowers the EP thermocline depth anomaly h_{E}. Through the thermocline feedback, $T^{\mathrm{E}}_{\mathrm{sub}}$ is further decreased, closing the loop. This feedback eventually diminishes due to the non-linear nature of the thermocline feedback as a deeper thermocline only marginally decreases the subsurface temperature. The direct wind feedback (center) connects the trade winds to the strength of upwelling and advection. This creates a second feedback loop that also amplifies the zonal SST gradient. Both feedbacks are eventually stopped by a lower limit for $T^{\mathrm{E}}_{\mathrm{sub}}$. (b) Visualization of the coordinate transformation of T_{r} and T_{r0} to reformulate the effect of climate change induced T_{r} increase. Exploiting the temperature translation invariance of the system, an increase of ΔT_{r} in T_{r} is equivalent to a decrease of ΔT_{r} in T_{r0}, as formulated in Equation (10).

The previous result has significant consequences as it marks an entry point to the feedback mechanism in Figure 7a. As the initial temperature difference between surface and subsurface increases, the model provides a larger cooling effect on the EP surface. This leads to a new mean state with an increased zonal SST difference (Figure 8a). Through Equation (9), this has a direct effect on the thermocline depths, with the WP thermocline deepening and the EP thermocline lifting, while the thermocline in the CP remains constant (Figure 8b). Since the working principle of this mechanism is qualitatively independent on the precise parameter values like ϵ and ζ in the ENSO model, this analysis is also qualitatively robust for different parameter sets than the one specified in Section 3.1, as long as the advection coupling between the WP and EP stays weak.

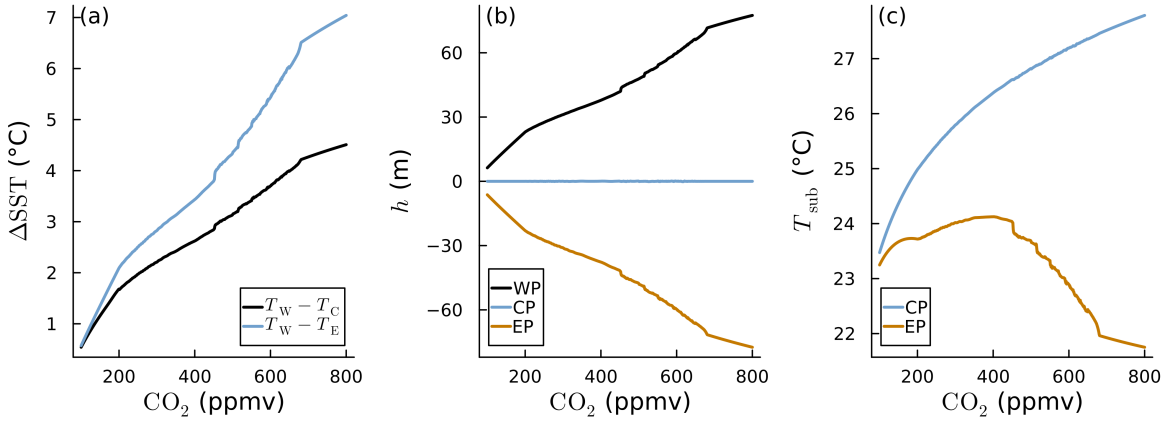

Figure 8: Mean states of selected variables for best estimate parameters as a function of CO_2 concentration. (a) Zonal temperature differences proportional to the wind stress over the central-western (black) and central (blue) Pacific. Positive values imply easterly winds. (b) Thermocline depth anomaly in the WP (h_W) as a direct output of the model, and in the CP (h_C) and EP (h_E) according to Equation (4). Equivalently, all mean thermocline depth anomalies can be calculated using Equation (9). (c) Subsurface temperatures following Equation (3) in the central (T^C_{sub}, blue) and eastern (T^E_{sub}, orange) Pacific.

With the stagnating thermocline in the CP, the corresponding subsurface temperature in Equation (3a) increases directly proportional to T_r (Figure 8c). Through that same mechanism, the EP subsurface temperature increases, too. However, linked to the shallowing thermocline h_E, the competing mechanism of the thermocline feedback that cools the subsurface plays a role here. Due to its non-linear nature, the thermocline feedback initially slows down the T_r related increase of T^E_{sub} (Equation (3b)), before it eventually surpasses the impact of T_r, leading to a decrease in T^E_{sub} after around 400 ppmv.

Through upwelling, changes in subsurface temperatures are reflected in the SST, leading to the similar shape of T_E and T^E_{sub}. However, this is not true for the CP due to the advection feedback in Equation (2b), which brings cool waters from the EP to the CP, decreasing T_C. This leads to a peculiar model behavior where the CP subsurface temperature surpasses the CP SST such that upwelling in that region now effectively warms the SST. This is evident in Figure 9b, where upwelling (gray) induces a net positive temperature flux in the CP. Only through the strong advection from the EP (dark blue), the shape of T_C is similar to that in the EP. As vertical temperature profiles in the tropical Pacific typically decrease with depth (Tsonis et al., 2003), this behavior seems unrealistic and must be deemed a model limitation that requires further improvement. However, the overall conclusions on the mean state are robust, as the feedback loop in Figure 7a only requires a weak coupling between the WP and EP which would also be given for a cooler CP with EP-like temperatures. In fact, the argument does not change even if a 2-box model without the CP, like the one from Timmermann et al. (2003), is considered.

Summarizing, in our model we observe an increasing zonal SST gradient for higher CO_2 concentrations which translates to strengthened trade winds and a steeper thermocline slope. Our analysis shows that the origin of this behavior lies in an initial cooling of the subsurface temperatures as a result of a climate change induced parameter shift. In other words, a warmer climate is directly impacting the subsurface by cooling it relative to the surface. The increased vertical temperature gradient then kicks off a positive feedback loop that increases the zonal SST gradient and defines a new mean state of the model.

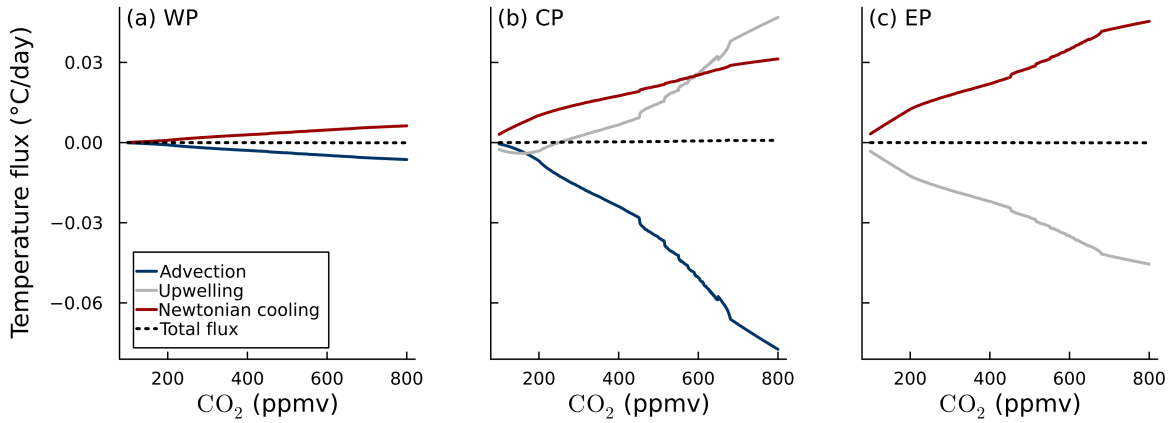

Figure 9: Mean state temperature fluxes in the WP (a), CP (b) and EP (c) for best estimate parameters as a function of CO_2 concentration. The equilibrium total flux of zero (dashed black) is separated into fluxes of advection (dark blue), upwelling (gray), and Newtonian cooling (red).

This opposes results from GCMs that generally project a lower zonal SST gradient due to the enhanced warming in the EP, and a weakening of the trade winds (W. Cai et al., 2021). However, ocean-atmosphere reanalysis recorded the opposite trend since 1980, which includes cooling of the eastern Pacific and a strengthening of the easterly winds (Alizadeh, 2024; W. Cai et al., 2021). While our model only shows a cooling of the EP from 450 ppm onwards, the zonal contrast and with that the easterlies exhibit a monotonic increase matching reanalysis.

Furthermore, a cooling trend of the EP subsurface is also observed in reanalysis data from 1979 to 2014 (Chung et al., 2019). Similarly, the 10 % of ensemble members from the Community Earth System Model (CESM) Large Ensemble Project that exhibit the most significant increase in Walker circulation also display a similar trend during that period, though at a smaller magnitude (Chung et al., 2019). Our analysis emphasizes the significance of EP subsurface temperatures response to climate change for the mean state of ENSO. The identified model mechanism, albeit highly parameterized, could provide a physical explanation of the observed strengthened Walker circulation that does not rely on internal variability or influences from outside the Pacific.

5.2 Characteristics of El Niño in a Changing Climate

With increasing CO_2 concentrations, the characteristics of El Niño in our model change significantly. Figure 10 shows the evolution of key features of El Niño in the Niño 3.4 region: (a) amplitude, (a) period and (c) variance. Panel (a) shows that both the maximum amplitude (gray) and the mean amplitude (blue) of an El Niño event rise significantly in a warmer climate, with maximum amplitudes of over 4 °C. The black dots in Figure 10a create an orbit diagram (Strogatz, 2015) of the coupled model that visualize the its oscillatory behavior. The Hopf bifurcations that are bounding the region of oscillatory model behavior for BE parameters are indicated by vertical dashed lines. The precise location of these bifurcation points is a function of the model parameters which explains the possibility of non-zero amplitudes of the MC mean outside of the region of periodic orbits. With increasing CO_2 concentrations, we can identify period doubling bifurcations in the orbit diagram, which are accompanied by short windows of chaotic behavior. The maximum amplitude increases step-wise with each bifurcation - a behavior that is smoothed out for the MC lines in gray and blue. At around 650 ppmv, this trend collapses and the system transfers back to periodic orbits with significantly lower amplitudes. The amplitudes then keep decreasing up to the Hopf bifurcation where the oscillation finally ceases.

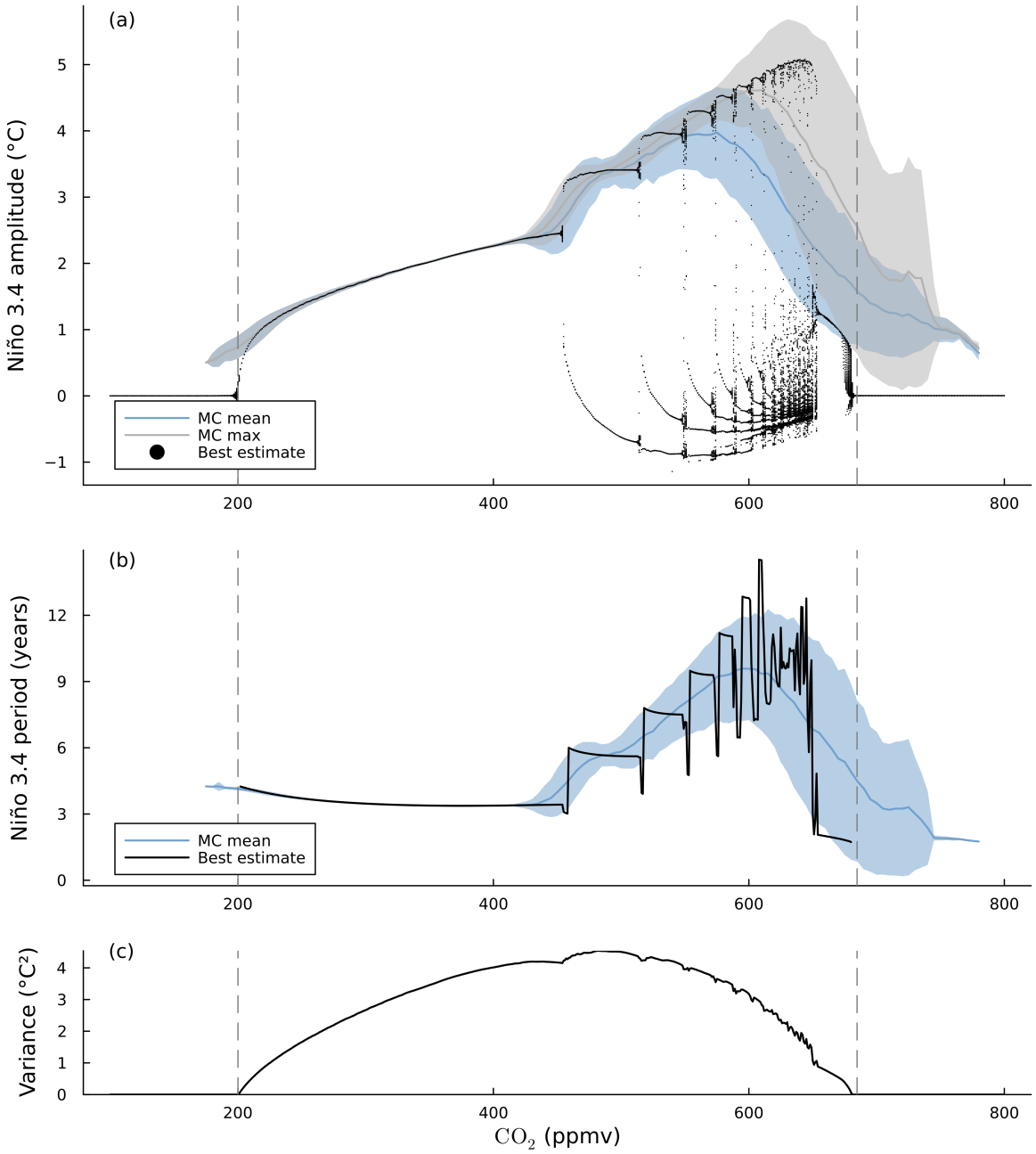

Figure 10: Key characteristics for the model Niño 3.4 index as a function of CO_2 concentrations. Vertical dashed lines indicate Hopf bifurcations for the best estimate parameter set. (a) Amplitudes of El Niño events defined as anomalies $\geq 0.4\,°C$. In gray, the maximum amplitude averaged over all MC simulations is shown, with the standard deviation indicated by the shaded ribbon. The same is shown for the mean amplitude of an El Niño event in blue. The black dots represent local maxima of simulation runs with best estimate parameters. As no prior filtering was applied, amplitudes $< 0.4\,°C$ or even in the negative regime are possible. (b) Average time between two El Niño events for the MC simulations in blue and the best estimate parameters in black. (c) Variance of the Niño 3.4 index for best estimate parameters.

At the same time, our model also shows a significant increase in the time between two El Niño events for higher CO_2 concentrations (Figure 10b). This implies that, while individual El Niño events become more extreme, they occur much less frequently. This leads to a rising variance until around 480 ppmv CO_2 after which it decreases again (Figure 10c). This is only partly in line with W. Cai et al. (2021), who find an overall inter-model consensus on increasing SST variability with increasing CO_2 concentrations. In summary, while we do not observe more frequent extreme El Niño events as in W. Cai et al. (2021), we do find that the events that occur in our model become more extreme in a warmer climate.

The changes in our model's ENSO characteristics might also affect how GMST responds to ENSO. This is discussed in the following section.

5.3 The Response of GMST to ENSO in a Changing Climate

As SSTs in the central and eastern Pacific rise during an El Niño event, energy fluxes into the atmosphere increase, thus increasing GMST in our coupled model. The response of GMST to anomalies in the Niño 3.4 region, i.e., the slope of the regression between Niño 3.4 index and delayed GMST stays fairly constant around 0.12 °C per degree of Niño 3.4 index for a large range of CO_2 concentrations (Figure 11a). Related to the chaotic windows discussed in the previous Subsection 5.2 the GMST response line for BE parameters is smooth for low CO_2 concentration, but shows discontinuities at higher concentrations, before collapsing at around 650 ppmv. The latter is connected to reduced Niño 3.4 amplitudes in this regime as visible in Figure 10, but the exact origin of this relationship requires further investigation.

The delay between ENSO and GMST, i.e., the time lag at maximum cross-correlation, is shown in Figure 11b. With increasing CO_2 concentrations, the lag time decreases, implying a faster response of GMST to ENSO. However, this decrease is very slow for current and future CO_2 concentrations and stays at a delay of about 4 months.

To put these findings into perspective, we turn to to literature and available reanalysis data. For the period 1950 to 1998, Trenberth et al. (2002) found a delay of 3 months between the Niño 3.4 index and GMST, slightly lower than our model results. They also quantified the GMST response and found regression coefficients of 0.11 °C per degree of Niño 3.4 index for the period of 1950-1978 and a weaker $0.08\,^{\circ}\mathrm{C}\,^{\circ}\mathrm{C}^{-1}$ for the period of 1979-1998. The drop in the slope was accompanied by a reduction of the correlation coefficient from 0.65 to about 0.43, which they attributed to either volcanic activity in the period of 1979-1998, the climate shift 1976/1977, or both.

Motivated by these results, based on reanalysis data we analyze the cross-correlation between the Niño 3.4 index and GMST in two periods: 1980-1998 and 1999-2023, respectively (Figure 12). Last century's period shows much lower peak correlation of 0.44 than the second period 1999-2023 which has a peak correlation of 0.69. This is in line with the findings of Trenberth et al. (2002), strongly suggesting that the two major eruptions at the end of the 20th century obscure the relationship. Both eruptions, El Chichón and Pinatubo, occurred during the onset of an El Niño event, weakening its perceived impact on GMST (Wigley, 2000). To circumvent this masking, we focus on the period of 1999-2023 where we find a regression coefficient of $(0.11 \pm 0.01)\,^{\circ}\mathrm{C}$ of GMST warming per degree of Niño 3.4 index. This is consistent with what was found in Trenberth et al. (2002) for the period of 1950-1978 and close to the $1.3\,^{\circ}\mathrm{C}\,^{\circ}\mathrm{C}^{-1}$ found in Wigley (2000). For reasons not yet fully understood, the regression coefficient of $0.6\,^{\circ}\mathrm{C}\,^{\circ}\mathrm{C}^{-1}$ for 1980-1998 found in our analysis is significantly lower than that of Trenberth et al. (2002) for the period of 1979-1998. This discrepancy might be due to the different time period and dataset considered, and depends on the exact definition of the Niño 3.4 index, the data processing and the implementation of the regression analysis.

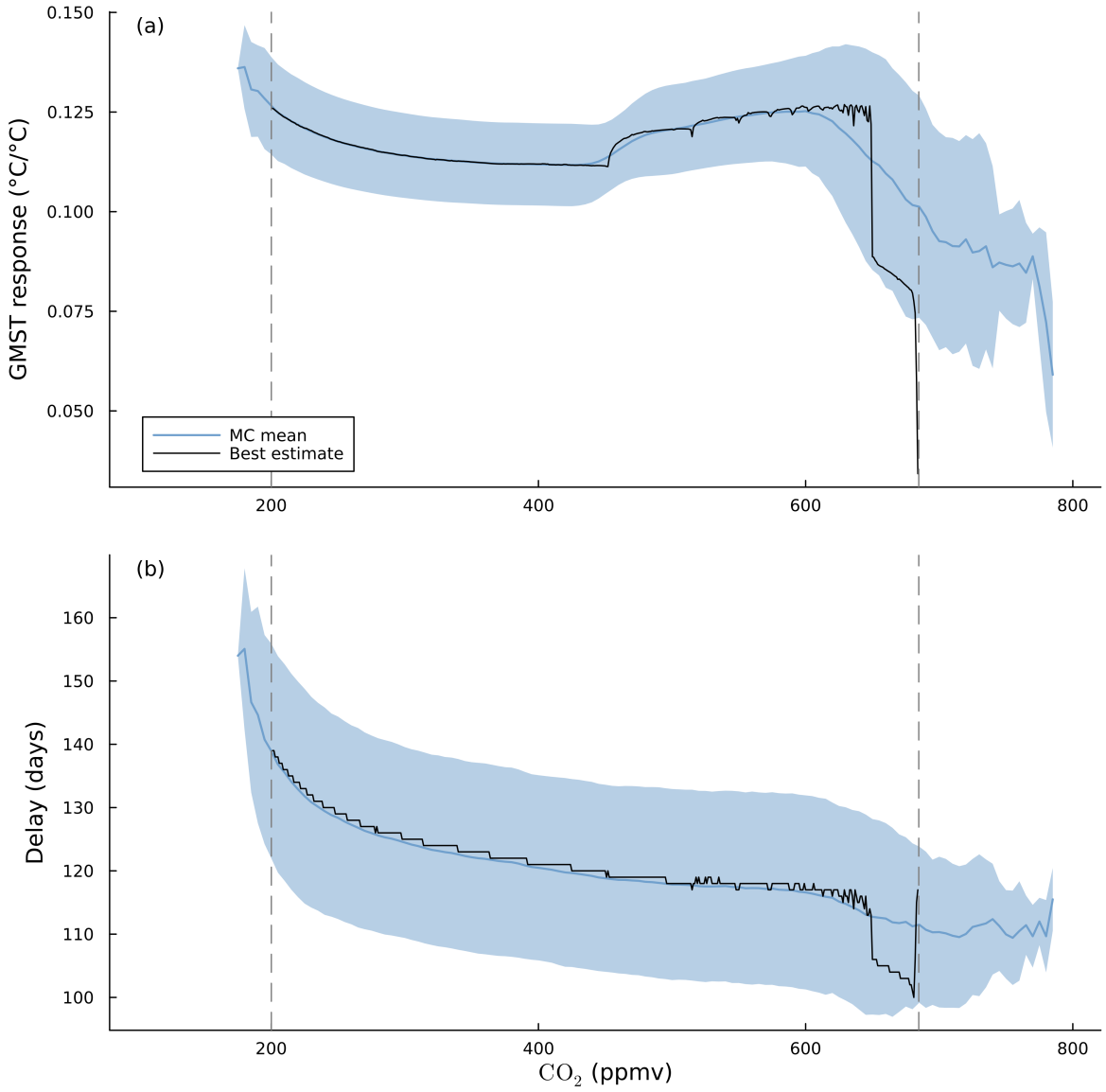

Figure 11: Key characteristics of GMST response to ENSO. Vertical dashed lines indicate Hopf bifurcations for the best estimate parameter set. (a) Regression coefficient of delayed GMST to Niño 3.4 index from the coupled model for different CO_2 concentrations. The blue line represents the mean of the MC samples with their standard deviation shaded. The black line is the result for best estimate parameters. (b) Time lag between Niño 3.4 index and GMST with maximum cross-correlation for different CO_2 concentrations that is used to delay GMST in the top panel. Colors are the same as in the top panel.

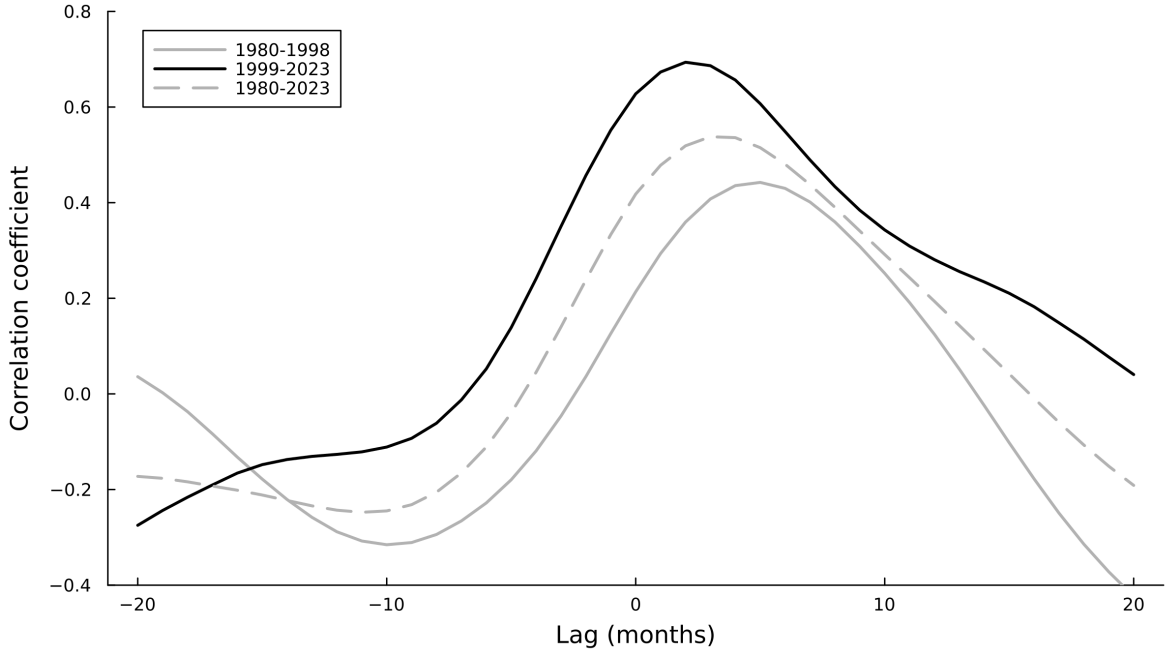

Figure 12: Cross-correlation between the Niño 3.4 index and GMST from reanalysis data for different periods. Positive lags indicate that Niño 3.4 index leads GMST. Depiction inspired by Trenberth et al. (2002).

In Figure 12, we find the peak correlation of the period 1999-2023 at a lag of only two months, lower than the 3 months found by Trenberth et al. (2002) for the period of 1950-1978. Note, however, that this does not necessarily support the trend of decreasing delay with increasing CO_2 concentrations found in our model as the peak both in Figure 12 and in the equivalent Figure 2 from Trenberth et al. (2002) is broad enough to support a delay range of between 2-3 months.

In summary, we find a linear GMST response to Niño 3.4 index of around 0.12 °C across a wide range of CO_2 concentrations in our model. This is supported by observations in our analysis, where we find (0.11 ± 0.01) °C for the period of 1999-2023 with low volcanic activity. Furthermore, Trenberth et al. (2002) finds a similar regression coefficient for 1950-1978, a period with similarly low volcanic activity. Hence, observational analysis does not contradict the relatively stable GMST response under changing CO_2 concentrations found in our model. In relation to the delay between Niño 3.4 index and GMST, our observational analysis and Trenberth et al. (2002) suggest a shorter delay than we find in our model, while Wigley (2000) uses a delay of 6-7 months. As Trenberth et al. (2002) points out, this could be a result of different methods to correct for the volcanic influence on GMST.

6 Conclusion and Discussion

In this research, we developed a full-field conceptual GMST model that responds to changes in CO_2 concentrations and SST variability in the tropical Pacific. Its physical formulation allows for interpretation and parameter verification against existing literature. Model parameters were optimized using observational data from 1980-2023. The model was coupled with a pre-existing ENSO model from Fang et al. (2024), which reproduces typical interannual SST variability in the western, central, and eastern Pacific. The achieved coupling is bidirectional: the GMST model takes SSTs from the ENSO model as input, allowing GMST to respond to temperature changes in the three Pacific boxes. In turn, the ENSO model is influenced by the GMST model through a key variable, the radiative-convective equilibrium temperature T_r. Assuming that the western Pacific SSTs are approximately in this equilibrium, T_r was linearly parameterized as a function of GMST. The coupled model is cost-effective to operate and allows for a detailed analysis of the interplay between ENSO and GMST.

Subsequently, the model's bidirectional relationship between ENSO and GMST was analyzed by exploring model solutions for different CO_2 concentrations between 100 and 800 ppmv. In the mean state, increased CO_2 concentration leads to a warming of GMST and western Pacific SST. However, central and eastern Pacific SSTs show a more complex response, initially warming slowly but decreasing from around 450 ppmv onwards. Exploiting the model's interpretable nature, we can separate the effect of climate change on the Pacific and its intra-basin dynamics. Our analysis shows that the observed behavior is a result of a warming GMST acting to decrease subsurface temperatures relative to the surface. This subsequently fuels a feedback loop constrained by bounding parameters and a new mean state with an enhanced zonal SST gradient is found. ENSO itself, as measured by the area-weighted Niño 3.4 index in our model, also changes in response to increased CO_2 concentration. In a warmer climate, El Niño events occur less frequently but are significantly stronger. The response of GMST to ENSO variability, however, stays approximately constant at around 0.12 °C per degree of Niño 3.4 index. This implies that larger excursions of GMST can be expected due to higher ENSO amplitudes, albeit at a lower frequency. At the same time, the response time of GMST to the Niño 3.4 index decreases with rising CO_2 concentrations. Nevertheless, the observed decrease is very low for current to future CO_2 concentrations and the delay remains close to 4 months.

While the simple structure of the coupled ENSO-GMST model allows for a cost-effective, isolated and interpretable exploration of the relationship between ENSO and GMST, the conceptual nature of both model components has its limitations. Many aspects of the GMST model drastically simplify the earth system and its internal feedback mechanisms. For instance, the model uses a single combined heat capacity for all individual forcing mechanisms (ENSO, CO_2, and AOD), which oversimplifies their distinct thermal dynamics. Additionally, for the response to Pacific variability, a linear relationship based on the difference between GMST and local SST difference was employed, an assumption that might not be universally valid. In particular, latent heat fluxes that dominate the heat exchange over the tropical oceans (Hoffert et al., 1983) are typically formulated to be dependent on humidity (e.g. Weaver et al. (2001)) - a variable not included in our model. Furthermore, particularly net radiation fluxes between ocean and atmosphere are heavily dependent on local cloud cover (Hartmann et al., 2001), but convection is not explicitly included in the model. Lastly, while the fitting of GMST model parameters to observations ensures a good representation of the current climate, it is unclear to what extent the model can project future climate states.

While the ENSO model incorporates many important feedbacks, it is only intended as a simple analogue representing the physics of ENSO, and cannot reproduce individual events realistically (Fang et al., 2024). Reasons for this include its spatial resolution bu also the lack of representation of some feedbacks. For example, the west-east damping differential leads to stronger regulation of the WP through evaporation and a greater net negative radiative cloud feedback (W. Cai et al., 2021), both of which are not part of the ENSO model. Additionally, although the model reveals rich dynamics, it does not capture effects from seasonal variability or relatively fast atmospheric processes. Possibly as a consequence of

these shortcomings, though the model can reproduces ENSO bursting behavior, it overestimates the relative occurrence of strong El Niño events (Timmermann et al., 2003). Consequently, the analysis in this study might be skewed towards exceptionally strong El Niño events rather than the average to weak El Niño event. Additionally, while the heavy parameterization keeps the model simple and interpretable, the parameterized relationships that are tailored to the current climate might not be valid for a future, warmer climate. This could lead to unrealistic model artifacts such as the observed unstable stratification in the CP mean state. Therefore, only adjusting key parameters such as T_r to represent a warmer climate might be insufficient as the parameterization itself might change due to climate change. Moreover, other parameters such as the sharpness of the thermocline h^* or its reference depth H might be subject to change. In this context, the linear parameterization used for T_r might not be universally valid, and is currently based solely on observational data.

Despite the model limitations, the coupled ENSO-GMST model developed in this study provides a valuable tool for understanding the bidirectional relationship between ENSO and GMST. Investigation of reanalysis data supports the modeled GMST response to ENSO, demonstrating our model's capability to capture the coupling from ENSO to GMST. In the opposite coupling direction from GMST to ENSO, our model shows increasing zonal SST gradients under climate change, a feature that is supported by reanalysis data but not seen in most projections from the Coupled Model Intercomparison Project Phase 6 (CMIP6) (W. Cai et al., 2021; Chung et al., 2019). We identified the central and eastern subsurface temperatures as the key driver of this behavior. Reanalysis suggests that these temperatures have been cooling in recent decades (Chung et al., 2019). This trend, as well as the decreasing EP sea surface temperatures can also be observed in our model from an inflection point at around 400 ppmv and 450 ppmv onwards, respectively. As the precise location of this inflection point is likely dependent on ENSO model parameters and tuning these might shift the inflection point to lower CO_2 concentrations, further improving the model alignment with reanalysis data. Hence, our model might be able to provide an intra-Pacific mechanism that explains the observed changes.

However, other model results such as the increased amplitude but decreased frequency of El Niño events in a warmer climate are not fully supported by the literature (W. Cai et al., 2021). This could be connected to the unstable stratification that developes in the mean state of the WP for higher CO_2 concentrations. Here, as the SST is lower than the corresponding subsurface, the upwelling feedback is perturbed, potentially deteriorating the model's ENSO behavior. Consequently, moving forward, it is essential to resolve this issue, for instance, by reformulating the subsurface temperature parameterization. Nevertheless, leveraging the model's interpretability, future research could explore the precise mechanisms that drive the observed ENSO trends and assess their validity. Additionally, this could include an analysis of the model's La Niña events, which was outside the scope of this work. Moreover, the current model setup is able to dynamically respond to changing CO_2 concentrations. Therefore, future research could exploit this capability and investigate the model response to transient CO_2 concentrations. The coupled model could be further used to explore the role of internal variability that has been proposed as a potential driver of the recent Walker circulation strengthening (W. Cai et al., 2021). For instance, to mimic the PDO, the advection efficiency ϵ could be varied, an increase of which would represent a decreasing PDO index (Fang et al., 2024).

In addition, as the GMST model was developed as a separate component of the coupled model, it could be applied to other ENSO models, in particular those influenced by high-frequency forcing. This could help assess the implications of different ENSO modeling approaches on the bidirectional relationship of ENSO and GMST. As part of this effort, the GMST could be further improved by training it using model data from GCM projections to improve its representation of a future climate. In this regard, training on models with equilibrated climates would also be possible and would expand the model's capabilities to a representation of equilibrated instead of transient climates. It should be noted, however, that both approaches bear the risk of inheriting ENSO-related model biases in particular, such as the cold tongue bias (W. Cai et al., 2021).

Instead of coupling the GMST with a different ENSO model, improvements to the current ENSO model could also be a potential way forward. For instance, the addition of noise to the wind stress terms in the ENSO model could be explored. This could potentially generate unique El Niño events, spur oscillations outside the regime of periodic orbits and also generate shorter-term variability in the GMST. Note, however, that this would still not be enough to reproduce the full spectrum of GMST variability as the global atmospheric variability is dominating these short-term fluctuations. Further improvement of the ENSO model could aim to resolve the lack of the west-east damping differential. A potential way of implementing this could be the use of distinct RCE temperatures in each basin with a unique response to GMST. This has the potential to improve the model's mean state representation and could possibly challenge our current results as this mechanism works to reduce the zonal SST difference (W. Cai et al., 2021). In this regard, the ENSO-to-GMST coupling could also be refined by introducing unique ocean-atmosphere coupling coefficients for each basin. This could potentially give insights into whether different ENSO flavors have distinct impacts on GMST.

In conclusion, the coupled ENSO-GMST model developed in this study provides a valuable tool for understanding the bidirectional relationship between ENSO and GMST. Leveraging its capabilities revealed a potential intra-Pacific mechanism resembling recent mean state changes of the tropical Pacific. Further research could validate these insights by further exploring the current model setup, improving the individual model components, or even coupling the GMST model to other ENSO models. Ultimately, this could further improve our understanding of the complex relationship between ENSO and GMST in an uncertain future climate.

References

Alizadeh, O. (2024). A review of ENSO teleconnections at present and under future global warming. *WIREs Climate Change*, *15*(1), e861. https://doi.org/10.1002/wcc.861

Bezanson, J., Edelman, A., Karpinski, S., & Shah, V. B. (2017). Julia: A Fresh Approach to Numerical Computing. *SIAM Rev.*, *59*(1), 65–98. https://doi.org/10.1137/141000671

Bjerknes, J. (1969). Atmospheric Teleconnections From The Equatorial Pacific. *Monthly Weather Review*, *97*(3), 163–172. https://doi.org/10.1175/1520-0493(1969)097<0163:ATFTEP>2.3.CO;2

Cai, M., Sun, J., Ding, F., Kang, W., & Hu, X. (2023). The Quasi-Linear Relation between Planetary Outgoing Longwave Radiation and Surface Temperature: A Climate Footprint of Radiative and Nonradiative Processes. *Journal of the Atmospheric Sciences*, *80*(9), 2131–2146. https://doi.org/10.1175/JAS-D-22-0261.1

Cai, W., Santoso, A., Collins, M., Dewitte, B., Karamperidou, C., Kug, J.-S., Lengaigne, M., McPhaden, M. J., Stuecker, M. F., Taschetto, A. S., Timmermann, A., Wu, L., Yeh, S.-W., Wang, G., Ng, B., Jia, F., Yang, Y., Ying, J., Zheng, X.-T., … Zhong, W. (2021). Changing El Niño–Southern Oscillation in a warming climate. *Nat Rev Earth Environ*, *2*(9), 628–644. https://doi.org/10.1038/s43017-021-00199-z

Cai, W., Santoso, A., Wang, G., Yeh, S.-W., An, S.-I., Cobb, K. M., Collins, M., Guilyardi, E., Jin, F.-F., Kug, J.-S., Lengaigne, M., McPhaden, M. J., Takahashi, K., Timmermann, A., Vecchi, G., Watanabe, M., & Wu, L. (2015). ENSO and greenhouse warming. *Nature Clim Change*, *5*(9), 849–859. https://doi.org/10.1038/nclimate2743

Chen, J., Genio, A. D. D., Carlson, B. E., & Bosilovich, M. G. (2008). The Spatiotemporal Structure of Twentieth-Century Climate Variations in Observations and Reanalyses. Part I: Long-Term Trend. *Journal of Climate*, *21*(11), 2611–2633. https://doi.org/10.1175/2007JCLI2011.1

Chung, E.-S., Timmermann, A., Soden, B. J., Ha, K.-J., Shi, L., & John, V. O. (2019). Reconciling opposing Walker circulation trends in observations and model projections. *Nat. Clim. Chang.*, *9*(5), 405–412. https://doi.org/10.1038/s41558-019-0446-4

Collins, M., An, S.-I., Cai, W., Ganachaud, A., Guilyardi, E., Jin, F.-F., Jochum, M., Lengaigne, M., Power, S., Timmermann, A., Vecchi, G., & Wittenberg, A. (2010). The impact of global warming on the tropical Pacific Ocean and El Niño. *Nature Geosci*, *3*(6), 391–397. https://doi.org/10.1038/ngeo868

Dijkstra, H. A. (2005). *Nonlinear physical oceanography: A dynamical systems approach to the large scale ocean circulation and El Niño* (2nd rev. and enlarged ed). Springer. https://doi.org/10.1007/1-4020-2263-8

Dijkstra, H. A. (2013, June 17). *Nonlinear Climate Dynamics* (1st ed.). Cambridge University Press. https://doi.org/10.1017/CBO9781139034135

Dijkstra, H. A. (2024). The role of conceptual models in climate research. *Physica D: Nonlinear Phenomena*, *457*, 133984. https://doi.org/10.1016/j.physd.2023.133984

Dijkstra, H. A., & Burgers, G. (2002). Fluid Dynamics of El Nino Variability. *Annu. Rev. Fluid Mech.*, *34*(1), 531–558. https://doi.org/10.1146/annurev.fluid.34.090501.144936

Falster, G., Konecky, B., Coats, S., & Stevenson, S. (2023). Forced changes in the Pacific Walker circulation over the past millennium. *Nature*, *622*(7981), 93–100. https://doi.org/10.1038/s41586-023-06447-0

Fang, X., Dijkstra, H., Wieners, C., & Guardamagna, F. (2024). A Nonlinear Full-Field Conceptual Model for ENSO Diversity. *Journal of Climate*, *37*(14), 3759–3774. https://doi.org/10.1175/JCLI-D-23-0382.1

Foster, G., & Rahmstorf, S. (2011). Global temperature evolution 1979–2010. *Environ. Res. Lett.*, *6*(4), 044022. https://doi.org/10.1088/1748-9326/6/4/044022

Global Modeling And Assimilation Office (GMAO). (2015). *MERRA-2 instM_2d_gas_Nx: 2d,Monthly mean,Instantaneous,Single-Level,Assimilation,Aerosol Optical Depth Analysis V5.12.4*. Greenbelt, MD, USA, Goddard Earth Sciences Data and Information Services Center (GES DISC).

https://doi.org/10.5067/XOGNBQEPLUC5
(Accessed on 2024, May 7).

Global Volcanism Program. (2024). *Volcanoes of the World (v. 5.2.0)*. Distributed by Smithsonian Institution, compiled by Venzke, E. https://doi.org/10.5479/si.GVP.VOTW5-2024.5.2

Goddard, L., & Dilley, M. (2005). El Niño: Catastrophe or Opportunity. *Journal of Climate*, *18*(5), 651–665. https://doi.org/10.1175/JCLI-3277.1

Hartmann, D. L., Moy, L. A., & Fu, Q. (2001). Tropical Convection and the Energy Balance at the Top of the Atmosphere. *Journal of Climate*, *14*(24), 4495–4511. https://doi.org/10.1175/1520-0442(2001)014<4495:TCATEB>2.0.CO;2

Hersbach, H., Bell, B., Berrisford, P., Horányi, A., Muñoz-Sabater, J., Nicolas, J., Peubey, C., Radu, R., Rozum, I., Schepers, D., Simmons, A., Soci, C., Dee, D., & Thépaut, J.-N. (2023). *ERA5 monthly averaged data on single levels from 1940 to present*. Copernicus Climate Change Service (C3S) Climate Data Store (CDS). https://doi.org/10.24381/cds.f17050d7
(Accessed on 2024, May 6).

Hoffert, M. I., Flannery, B. P., Callegari, A. J., Hsieh, C. T., & Wiscombe, W. (1983). Evaporation-Limited Tropical Temperatures as a Constraint on Climate Sensitivity. *Journal of the Atmospheric Sciences*, *40*(7), 1659–1668. https://doi.org/10.1175/1520-0469(1983)040<1659:ELTTAA>2.0.CO;2

Hsu, C.-W., & Yin, J. (2019). How likely is an El Niño to break the global mean surface temperature record during the 21st century? *Environ. Res. Lett.*, *14*(9), 094017. https://doi.org/10.1088/1748-9326/ab3b82

Hu, S., & Fedorov, A. V. (2017). The extreme El Niño of 2015–2016 and the end of global warming hiatus. *Geophysical Research Letters*, *44*(8), 3816–3824. https://doi.org/10.1002/2017GL072908

IPCC. (2023). The Earth's Energy Budget, Climate Feedbacks, and Climate Sensitivity. In *Climate Change 2021: The Physical Science Basis. Contribution of Working Group I to the Sixth Assessment Report of the Intergovernmental Panel on Climate Change* (1st ed.). Cambridge University Press. https://doi.org/10.1017/9781009157896.009

Jacques-Coper, M., & Garreaud, R. D. (2015). Characterization of the 1970s climate shift in South America. *International Journal of Climatology*, *35*(8), 2164–2179. https://doi.org/10.1002/joc.4120

Jakob, C., Singh, M. S., & Jungandreas, L. (2019). Radiative Convective Equilibrium and Organized Convection: An Observational Perspective. *Journal of Geophysical Research: Atmospheres*, *124*(10), 5418–5430. https://doi.org/10.1029/2018JD030092

Jin, F.-F. (1997). An Equatorial Ocean Recharge Paradigm for ENSO. Part I: Conceptual Model. *J. Atmos. Sci.*, *54*(7), 811–829. https://doi.org/10.1175/1520-0469(1997)054<0811:AEORPF>2.0.CO;2

Jin, F.-F. (1996). Tropical Ocean-Atmosphere Interaction, the Pacific Cold Tongue, and the El Niño-Southern Oscillation. *Science*, *274*(5284), 76–78. Retrieved January 26, 2024, from https://www.jstor.org/stable/2891856

Koll, D. D. B., & Cronin, T. W. (2018). Earth's outgoing longwave radiation linear due to H $_2$ O greenhouse effect. *Proc. Natl. Acad. Sci. U.S.A.*, *115*(41), 10293–10298. https://doi.org/10.1073/pnas.1809868115

Kosovelj, K., & Zaplotnik, Ž. (2023). Indices of Pacific Walker Circulation Strength. *Atmosphere*, *14*(2), 397. https://doi.org/10.3390/atmos14020397

Lan, X., Tans, P., & Thoning, K. (2023). *Trends in globally-averaged CO2 determined from NOAA Global Monitoring Laboratory measurements*. (Version 2024-04). NOAA Global Monitoring Laboratory. https://doi.org/10.15138/9N0H-ZH07

McGregor, S., Timmermann, A., Stuecker, M. F., England, M. H., Merrifield, M., Jin, F.-F., & Chikamoto, Y. (2014). Recent Walker circulation strengthening and Pacific cooling amplified by Atlantic warming. *Nature Clim Change*, *4*(10), 888–892. https://doi.org/10.1038/nclimate2330

Newell, R. E. (1986). El Niño: An Approach Towards Equilibrium Temperature in the Tropical Eastern Pacific. *Journal of Physical Oceanography*, *16*(7), 1338–1342. https://doi.org/10.1175/1520-0485(1986)016<1338:ENAATE>2.0.CO;2

Newell, R. E., & Dopplick, T. G. (1979). Questions Concerning the Possible Influence of Anthropogenic CO2 on Atmospheric Temperature. *Journal of Applied Meteorology and Climatology*, *18*(6), 822–825. https://doi.org/10.1175/1520-0450(1979)018<0822:QCTPIO>2.0.CO;2

NOAA. (2022, June 3). *Carbon dioxide now more than 50% higher than pre-industrial levels*. Retrieved April 17, 2024, from https://www.noaa.gov/news-release/carbon-dioxide-now-more-than-50-higher-than-pre-industrial-levels

North, G. R. (1975). Theory of Energy-Balance Climate Models. *Journal of the Atmospheric Sciences*, *32*(11), 2033–2043. https://doi.org/10.1175/1520-0469(1975)032<2033:TOEBCM>2.0.CO;2

Rackauckas, C., & Nie, Q. (2017). DifferentialEquations.jl – A Performant and Feature-Rich Ecosystem for Solving Differential Equations in Julia. *Journal of Open Research Software*, *5*(1). https://doi.org/10.5334/jors.151

Singh, A. (2012). *Contrasting the flavors of ENSO and related trends in the tropical Pacific Ocean in recent decades*. https://theses.hal.science/tel-00795552

Smith, C. J., Kramer, R. J., Myhre, G., Forster, P. M., Soden, B. J., Andrews, T., Boucher, O., Faluvegi, G., Fläschner, D., Hodnebrog, Ø., Kasoar, M., Kharin, V., Kirkevåg, A., Lamarque, J.-F., Mülmenstädt, J., Olivié, D., Richardson, T., Samset, B. H., Shindell, D., ... Watson-Parris, D. (2018). Understanding Rapid Adjustments to Diverse Forcing Agents. *Geophysical Research Letters*, *45*(21), 12, 023–12, 031. https://doi.org/10.1029/2018GL079826

Strogatz, S. H. (2015). *Nonlinear dynamics and chaos: With applications to physics, biology, chemistry, and engineering* (Second edition). Westview Press, a member of the Perseus Books Group. https://doi.org/10.1201/9780429492563

Su, J., Zhang, R., & Wang, H. (2017). Consecutive record-breaking high temperatures marked the handover from hiatus to accelerated warming. *Sci Rep*, *7*(1), 43735. https://doi.org/10.1038/srep43735

Sun, D.-Z. (2000). Global climate change and ENSO: A theoretical framework. In H. F. Diaz & V. Markgraf (Eds.), *El Niño and the Southern oscillation*. Cambridge university press.

Tang, Y., Zhang, R.-H., Liu, T., Duan, W., Yang, D., Zheng, F., Ren, H., Lian, T., Gao, C., Chen, D., & Mu, M. (2018). Progress in ENSO prediction and predictability study. *National Science Review*, *5*(6), 826–839. https://doi.org/10.1093/nsr/nwy105

Thermtest. (n.d.). *Materials Thermal Properties Database*. Retrieved June 20, 2024, from https://thermtest.com/thermal-resources/materials-database

Thompson, D. W. J., Wallace, J. M., Jones, P. D., & Kennedy, J. J. (2009). Identifying Signatures of Natural Climate Variability in Time Series of Global-Mean Surface Temperature: Methodology and Insights. *Journal of Climate*, *22*(22), 6120–6141. https://doi.org/10.1175/2009JCLI3089.1

Timmermann, A., Jin, F.-F., & Abshagen, J. (2003). A Nonlinear Theory for El Niño Bursting. *J. Atmos. Sci.*, *60*(1), 152–165. https://doi.org/10.1175/1520-0469(2003)060<0152:ANTFEN>2.0.CO;2

Torrence, C., & Compo, G. P. (1998). A Practical Guide to Wavelet Analysis. *Bulletin of the American Meteorological Society*, *79*(1), 61–78. https://doi.org/10.1175/1520-0477(1998)079<0061:APGTWA>2.0.CO;2

Trenberth, K. E. (1997). The Definition of El Niño. *Bulletin of the American Meteorological Society*, *78*(12), 2771–2778. https://doi.org/10.1175/1520-0477(1997)078<2771:TDOENO>2.0.CO;2

Trenberth, K. E., Caron, J. M., Stepaniak, D. P., & Worley, S. (2002). Evolution of El Niño–Southern Oscillation and global atmospheric surface temperatures. *J.-Geophys.-Res.*, *107*(D8). https://doi.org/10.1029/2000JD000298

Tsonis, A. A., Hunt, A. G., & Elsner, J. B. (2003). On the relation between ENSO and global climate change. *Meteorology and Atmospheric Physics*, *84*(3-4), 229–242. https://doi.org/10.1007/s00703-003-0001-7

Veltz, R. (2020, July). Bifurcationkit.jl. *Inria Sophia-Antipolis*. https://hal.archives-ouvertes.fr/hal-02902346

Wang, C. (2018). A review of ENSO theories. *National Science Review*, *5*(6), 813–825. https://doi.org/10.1093/nsr/nwy104

Weaver, A. J., Eby, M., Wiebe, E. C., Bitz, C. M., Duffy, P. B., Ewen, T. L., Fanning, A. F., Holland, M. M., MacFadyen, A., Matthews, H. D., Meissner, K. J., Saenko, O., Schmittner, A., Wang, H., & Yoshimori, M. (2001). The UVic earth system climate model: Model description, climatology, and applications to past, present and future climates. *Atmosphere-Ocean*, *39*(4), 361–428. https://doi.org/10.1080/07055900.2001.9649686

Wigley, T. M. L. (2000). ENSO, volcanoes and record-breaking temperatures. *Geophysical Research Letters*, *27*(24), 4101–4104. https://doi.org/10.1029/2000GL012159

Yulaeva, E., & Wallace, J. M. (1994). The Signature of ENSO in Global Temperature and Precipitation Fields Derived from the Microwave Sounding Unit. *Journal of Climate*, *7*, 1719–1736. https://doi.org/10.1175/1520-0442(1994)007<1719:TSOEIG>2.0.CO;2

Zebiak, S. E., & Cane, M. A. (1987). A Model El Nino–Southern Oscillation. *Monthly Weather Review*, *115*(10), 2262–2278. https://doi.org/10.1175/1520-0493(1987)115<2262:AMENO>2.0.CO;2

Zhao, X., & Allen, R. J. (2019). Strengthening of the Walker Circulation in recent decades and the role of natural sea surface temperature variability. *Environ. Res. Commun.*, *1*(2), 021003. https://doi.org/10.1088/2515-7620/ab0dab